

The Optical Transition Radiation Monitor for
T2K: Studying Light Camera Gain, Motor
Controls and Disk studies from Simulations

Leif Z. R. Stawnyczy

Dec 19, 2008

Contents

1	Tokai to Kamioka: a Neutrino Beamline Experiment	3
1.1	Neutrino Mixing and the PMNS Matrix	4
1.2	T2K	6
1.2.1	Horns	8
1.2.2	Near Detector	8
1.2.3	Super K	10
1.2.4	Data Acquisition at SuperK	13
1.2.5	What to look for	13
1.3	Beam Monitoring System	15
1.3.1	Optical Transition Radiation System	16
1.3.2	OTR system design	17
2	Camera Gain	20
2.1	Camera	20
2.1.1	Camera Pedestal	21
2.2	Finding the Gain Curve	21
2.2.1	Analysis	26
2.3	Camera 2	28
2.3.1	Analysis of Camera 2	28
2.4	Additional Work on Camera Gain	30
2.5	Gain Corrections	30
3	Motor Controls	31
3.1	Motors	31
3.1.1	Arm Motor	32
3.2	Motor Motion	33
3.2.1	Fixed Rotation	33
3.2.2	Home Switch	33
3.2.3	Pressure Sensor	36
3.3	Conclusions	37
4	Simulations in Fluka	41
4.1	Evaluation	41
4.2	Conclusions	43

Chapter 1

Tokai to Kamioka: a Neutrino Beamline Experiment

The standard model is one of the best models in the physical sciences, but it is far from complete. Particle-antiparticle asymmetry, the generation problem for quarks and leptons (why are there three?), how are their masses and mixing determined and are the quarks and leptons unified at ultra-high energies: these are all questions that may be related but are currently not included in the standard model.

Currently in the standard model, neutrinos are assumed to have no mass, though this is not a theoretically predicted phenomenon. No mass for neutrinos means that neutrinos can't oscillate (see Section 1.1). However, this is not compatible with what has been observed in nature. The oscillation of neutrinos has been well established by other neutrino experiments in the past. While these experiments had found reasonable approximations of most of the mixing parameters, there is still much improvement to be made (see Section 1.1).

The T2K (T(okai) to K(amioka)) experiment will probe neutrino oscillations by utilizing the newly built Japan Proton Accelerator Research Complex (JPARC) in Tokai and the established (but recently renovated) facilities of SuperK in Kamioka. T2K will be looking at the disappearance of muon neutrinos as they oscillate into tau and electron neutrinos. The experiment consists of a fixed target collider and two detectors to observe the results, a "near detector" at 280m from the target and another "far detector" (SuperK) 300km away.

To ensure proper positioning of the proton beam, a number of beam monitoring systems have been included in the design. The Optical Transition Radiation (OTR) system, which will be discussed in more detail in section 1.3.1, is one such system - the last one before the target. When the proton beam crosses the boundary from one material to another, optical transition radiation is given off. By inserting a thin foil into the beam path and observing the emitted OTR ra-

diation through the use of a stage-mounted movable camera, the OTR team will get a good understanding of the beam’s characteristics. Because the precision of the beam measurements are directly related to how well one understands the characteristics of the camera, it was thereby necessary to thoroughly study this aspect of the system (See Chapter 2).

Due to the high radiation of the beam, the foils used in the OTR system may degrade over time. As a result, the OTR system has been equipped with a number of foils, each mounted on a disk that will rotate the necessary foil into position. Because of the radiation near the beam and the accuracy required in positioning the foils and camera, an automated motor system was included with the system and a user friendly interface was designed to allow ease of access and control for the user (See Chapter 3).

Lastly, while the effects of a thin foil inserted into the beam path would be negligible, the effects of the much thicker foil disk becoming stuck in the beam path (if the motion systems fail) may have potentially adverse side effects to the target. To this end, simulations were run to test the effects of just such an occurrence to see if it would be advisable to include a fail safe that would drop the foil disk away in the event that it should get stuck (See Chapter 4).

1.1 Neutrino Mixing and the PMNS Matrix

Neutrinos are electrically neutral particles that interact only via the weak force. There are known to be three types or “flavours” of neutrinos: the electron neutrino, the muon neutrino and the tau neutrino. These three neutrinos along with the electron, muon and tau particles make up the lepton “family” of particles in the Standard Model (SM).

While the SM assumes no neutrino mass, the consequence of observed neutrino oscillations, whereby one neutrino flavour oscillates into another, means that neutrinos do in fact have mass and that the SM as it is, is incomplete.

Neutrino mixing is described by a unitary 3×3 matrix called the Pontecorvo-Maki-Nakagawa-Sakata (PMNS) matrix such that:

$$|\nu_\alpha\rangle = \sum_i U_{\alpha i}^* |\nu_i\rangle \quad (1.1)$$

The ν_α correspond to the neutrino flavour states (electron, muon or tau) while the ν_i correspond to the neutrino mass eigenstates. The three mass eigenstates are composed of a mixture of the three neutrino flavours but have a definite mass associated with them - in other words, these are the “real” neutrinos. This difference between the mass eigenstates and the observed flavour states is the reason for neutrino oscillation.

The PMNS matrix itself is a product of three rotation matrices with three mixing angles, θ_{12} , θ_{23} and θ_{13} , and a complex phase, δ , and is given by:

$$U = \begin{pmatrix} 1 & 0 & 0 \\ 0 & c_{23} & s_{23} \\ 0 & -s_{23} & c_{23} \end{pmatrix} \begin{pmatrix} c_{13} & 0 & s_{13}e^{-i\delta} \\ 0 & 1 & 0 \\ -s_{13}e^{i\delta} & 0 & c_{13} \end{pmatrix} \begin{pmatrix} c_{12} & s_{12} & 0 \\ -s_{12} & c_{12} & 0 \\ 0 & 0 & 1 \end{pmatrix}$$

$$\begin{array}{c}
\nu_1 \qquad \qquad \qquad \nu_2 \qquad \qquad \qquad \nu_3 \\
= \begin{array}{c} \nu_e \\ \nu_\mu \\ \nu_\tau \end{array} \begin{pmatrix} c_{12}c_{13} & s_{12}c_{13} & s_{13}e^{-i\delta} \\ -s_{12}c_{23} - c_{12}s_{23}s_{13}e^{i\delta} & c_{12}c_{23} - s_{12}s_{23}s_{13}e^{i\delta} & s_{23}c_{13} \\ s_{12}s_{23} - c_{12}c_{23}s_{13}e^{i\delta} & -c_{12}s_{23} - s_{12}c_{23}s_{13}e^{i\delta} & c_{23}c_{13} \end{pmatrix} \quad (1.2)
\end{array}$$

where $c_{ij} \equiv \cos \theta_{ij}$ and $s_{ij} \equiv \sin \theta_{ij}$. The phase δ is a potential CP violating phase and becomes $-\delta$ for anti-neutrinos.

Thus the probability of a neutrino in flavour state α oscillating into flavour state β ($\alpha \neq \beta$) after a distance L is given by the formula:

$$\begin{aligned}
P(\nu_\alpha \rightarrow \nu_\beta) &= 4\{|U_{\alpha 3}U_{\beta 3}|^2 \sin^2 \Delta_{31} + |U_{\alpha 2}U_{\beta 2}|^2 \sin^2 \Delta_{21} \\
&\quad + 2|U_{\alpha 3}U_{\beta 3}U_{\alpha 2}U_{\beta 2}| \sin \Delta_{31} \sin \Delta_{21} \cos(\Delta_{32} + \delta)\} \quad (1.3)
\end{aligned}$$

where the unit-less phase Δ_{ij} is given by

$$\begin{aligned}
\Delta_{ij} &= \frac{c^3 L}{4\hbar E} \Delta m_{ij}^2 \\
&= \frac{GeV fm}{4\hbar c} * \frac{\Delta m_{ij}^2}{eV^2} \frac{L}{km} \frac{GeV}{E} \\
&= \frac{10^9 eV * 10^{-15} m}{4 * 6.582 * 10^{-16} eVs * 3 * 10^8 m/s} \frac{\Delta m_{ij}^2}{eV^2} \frac{L}{km} \frac{GeV}{E} \\
&\simeq 1.27 \frac{L(km)}{E(GeV)} \Delta m_{ij}^2 (eV^2) \quad (1.4)
\end{aligned}$$

As can be seen in 1.4, the probability of neutrino oscillation is a function of both the distance, L , over which it has travelled and the energy, E , that it has. It is important to note that the ratio L/E is the important ratio to consider when looking for neutrino oscillations. Because there are only three generations of neutrinos and since $\Delta m_{12}^2 + \Delta m_{23}^2 + \Delta m_{31}^2 = 0$ we only need two Δm^2 , three mixing angles (θ_{12} , θ_{23} , θ_{13}) and the phase (δ) to describe neutrino oscillation. The Δm^2 values used are those suggested by solar and atmospheric neutrino measurements: $\Delta m_{12}^2 \equiv \Delta m_{sol}^2 \approx 10^{-4} \rightarrow 10^{-5} eV^2$ and $\Delta m_{23}^2 \approx \Delta m_{31}^2 \equiv \Delta m_{atm}^2 \approx (1.6 \rightarrow 4) * 10^{-3} eV^2$. For $E \approx \Delta m_{23}^2 * L$ as in T2K ($E \approx 0.7 GeV$, $L = 295 km$), the Δm_{23}^2 terms dominate and 1.3 simplifies to:

$$\begin{aligned}
P_{\mu\tau} \equiv P(\nu_\mu \rightarrow \nu_\tau) &\simeq 4|U_{\mu 3}U_{\tau 3}|^2 \sin^2 \left(\frac{1.27 \Delta m_{atm}^2 L}{E} \right) \\
&= \sin^2 2\theta_{23} \cos^4 \theta_{13} \sin^2 \left(\frac{1.27 \Delta m_{atm}^2 L}{E} \right) \quad (1.5)
\end{aligned}$$

$$\begin{aligned}
P_{\mu e} \equiv P(\nu_\mu \rightarrow \nu_e) &\simeq 4|U_{\mu 3}U_{e 3}|^2 \sin^2 \left(\frac{1.27 \Delta m_{atm}^2 L}{E} \right) \\
&= \sin^2 \theta_{23} \sin^2 2\theta_{13} \sin^2 \left(\frac{1.27 \Delta m_{atm}^2 L}{E} \right) \quad (1.6)
\end{aligned}$$

Neutrino	Upper Limit
ν_e	3 eV
ν_{mu}	170keV
ν_{tau}	18.2MeV

Table 1.1: Neutrino flavours and the known upper bounds on their masses [14].

$$\begin{aligned}
P_{\mu\mu} &= 1 - P_{\mu\tau} - P_{\mu e} \\
&\simeq 1 - 4 \sin^2 \theta_{23} \cos^2 \theta_{13} (\cos^2 \theta_{23} \cos^2 \theta_{13} \\
&\quad + \sin^2 \theta_{13}) \sin^2 \left(\frac{1.27 \Delta m_{atm}^2 L}{E} \right)
\end{aligned} \tag{1.7}$$

From here, it is straight forward to see that for the *current* Standard Model ($m_\nu = 0$ and hence $\Delta m_{atm}^2 = 0$), the probabilities in equations 1.5 and 1.6 (ie, probability of a muon neutrino going to a tau or electron neutrino respectively) become 0 and no oscillation occurs. Since this isn't what's observed, there is need to expand the standard model to include neutrino mass.

Current experiments have placed upper limits on the masses of the various neutrino flavours (See Table 1.1), but there is still work to be done.

The primary goals of T2K are two-fold: by looking at the probability of muon neutrino disappearance (Equation 1.7), it will 1) find θ_{23} to within 1% precision and Δm_{23}^2 to better than 10^{-4} eV and 2) find the θ_{13} mixing angle to within more than an order of magnitude better sensitivity than previous experiments [13]. Current limits on θ_{13} and θ_{23} are such that $\sin^2 2\theta_{23} > 0.92$ and $\sin^2 2\theta_{13} < 0.19$ to within a 90% confidence interval [2].

1.2 T2K

The T2K (T(okai) to K(amioka)) experiment will probe neutrino oscillations by utilizing the newly built Japan Proton Accelerator Research Complex (JPARC) in Tokai and the established (but recently renovated) facilities of SuperK in Kamioka. The experiment will consist of a fixed target collider and two detectors to observe the results: a “near detector” at 280m from the target and another “far detector” (SuperK) 295km away.

Using JHFs 50GeV Proton Synchrotron (PS), a proton beam can be extracted and aimed at a stationary production graphite target, creating a shower of pions, kaons and other secondary particles which are then refocused using a series of electromagnetic horns (see Section 1.2.1) before they decay in an 80m decay pipe [13].

The beam is a 50GeV proton beam that delivers 3.3×10^{14} protons per pulse (ppp) at a repetition rate of 0.292 Hz. The power of the beam is 0.77MW (2.64 MJ/pulse) with a spill width of about 5.2 microseconds with about 8-15 buckets per spill [13]. However, at start up, the beam is only expected to be about 30GeV. In a typical year of operation (130 days), one expects to have 10^{21}

protons on target. The proton beam will be aimed toward a 30mm diameter, 900mm long cylindrical graphite target.

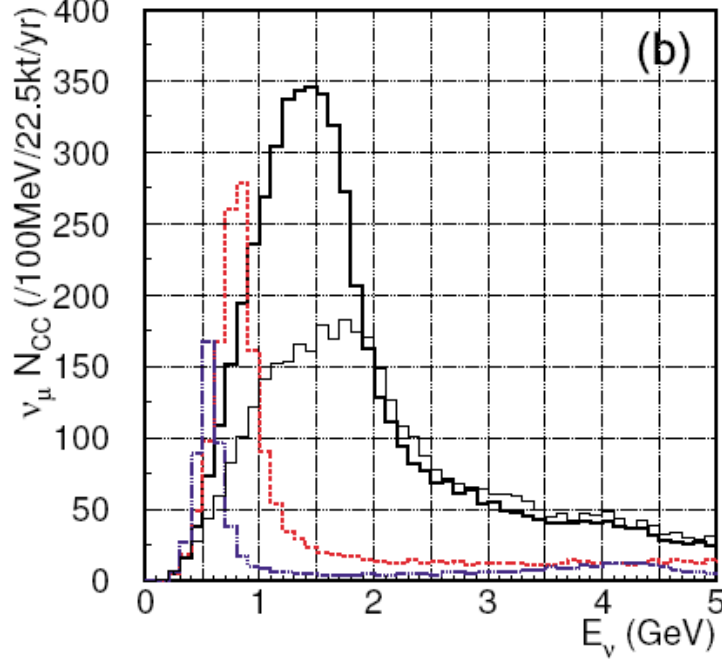


Figure 1.1: Neutrino energy histogram of number of charged current interactions (described in Section 1.2.5) for a proton beam configuration that is: thick - off-axis 1° , dashed - off-axis 2° and dotted - off-axis 3° . The thin solid line corresponds to a wide band beam configuration - an on-axis beam configuration that is not going to be implemented and hence not discussed here. This figure comes from [13].

Incidentally, the goal is not to have the beam aimed exactly on-axis of the far detector, but instead to have it aimed slightly off-axis. Figure 1.1 shows the results of Monte-Carlo simulations of expected neutrinos for beams aimed off axis by 1, 2 and 3 degrees [13]. The greatest flux (particles per unit area per second) of 0.7GeV neutrinos occurs when the beam is aimed off-axis by 2.5° .

The other benefit of aiming the beam off-axis is that there will be less electron neutrino contamination in the far detector (ie, a “purer” muon neutrino beam) because of the kinematics of the processes that produce electron neutrinos. Further, there will be fewer high energy neutrinos that do not contribute to signal, but do contribute to background noise (eg, $\pi^0 \rightarrow 2\gamma$ can sometimes be mistaken for electrons from ν_e interactions - see Figure 1.7 later).

1.2.1 Horns

There are three horns that will be used to refocus the secondary particles. Because most neutrinos are produced in the well-known two body decay of pions

$$\pi^+ \rightarrow \mu^+ + \nu_\mu \quad (1.8)$$

the horns are designed to focus the pions to achieve the desired neutrino energy (Section 1.1). The energy of the resultant neutrino beam is determined by

$$E_\nu = \frac{1}{2} \frac{m_\pi^2 - m_\mu^2}{E_\pi - p_\pi \cos \theta} \quad (1.9)$$

where E_π , p_π and m_π are the energy, momentum and rest mass of the pion, m_μ is the rest mass of the resultant muon (see equation 1.8 above) and θ is the angle between the neutrino and muon in the laboratory frame [14].

The horns are driven by a 320 kA pulsed current that is synchronized with the beam. The target itself will be located within the first horn while horns 2 and 3 will be located further downstream.

1.2.2 Near Detector

In order to measure ν_μ disappearance, it is important to first understand the flux of the ν_μ beam. For this, T2K uses a near detector located 280m downstream of the target. The near detector will measure the neutrino beam's flavour content, flux and other attributes before the neutrinos have a chance to oscillate.

In order to measure the neutrino flux, the ND280 is composed of the following components:

Magnet Used to measure the momenta of penetrating (charged) particles produced in neutrino interactions.

π^0 **Detector** Measures neutral current π^0 production. Composed of scintillating bars alternated with lead foil as well as inactive layers of water to measure interactions with oxygen - important for comparison to SuperK later.

Tracker Used to measure momenta of charged particles produced in charged current (CC) interactions and to measure ν_e background. It will be composed of 3 Time Projection Chambers (TPCs) and 2 Fine Grained Detectors (FGDs).

TPCs Used to measure momenta of muons produced within by charged current interactions. They will also be able to determine the signs of charged particles, identifying muons, pions and electrons. They will provide the most accurate measurement of the neutrino energy spectrum.

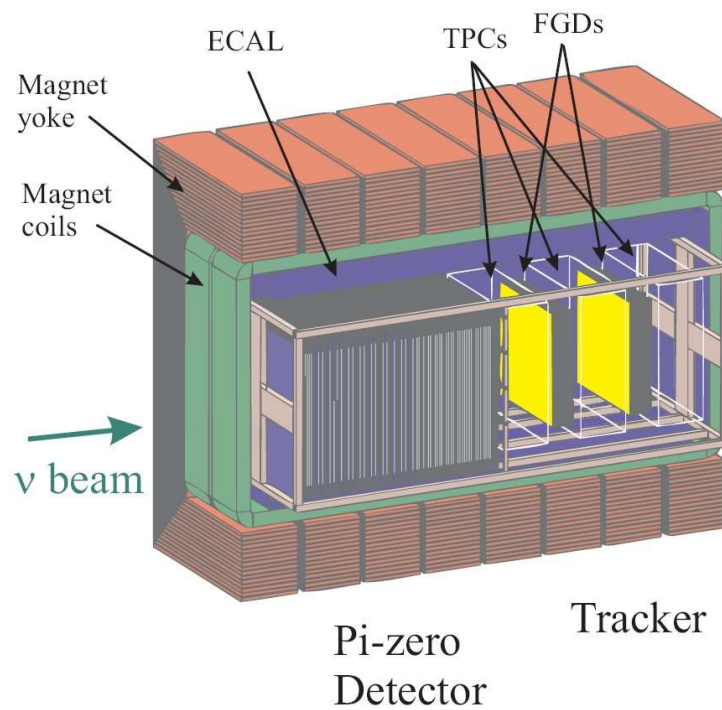


Figure 1.2: Diagram of ND280 and its various components. This figure comes from [8].

FGDs Placed between the TPCs, they will measure the direction and range of recoil protons from charged current interactions. While both will be composed of plastic scintillator, the second will include water to give an idea of the neutrino cross-section in water.

Electromagnetic calorimeter (Ecal) A segmented lead-scintillator detector used to measure the γ -rays produced that do not convert in the inner detectors and are used for reconstructing π^0 decays.

Side Muon Range Detector (SMRD) Air gaps at the side of the magnet are instrumented with scintillator to measure the range of muons that exit the detector. This can also be used as a sort of veto for events entering the detector.

The above features are all indicated in figure 1.2 above. Once the beam passes through the ND280, it then continues on for almost 300km to a detector located in the far west mines of Kamioka, Japan: SuperK.

1.2.3 Super K

Super Kamiokande, or SuperK, is a massive 50 thousand ton water Čerenkov radiation detector. Čerenkov radiation results when a charged particle travels through a medium faster than the speed of light in that medium. When a relativistic particle (ie, one travelling close to the speed of light) enters a medium with velocity

$$v_p = \beta c \quad (1.10)$$

greater than the speed of light in that same medium

$$v_{light} = c/n \quad (1.11)$$

n the index of refraction for the medium, a shock wave of electromagnetic radiation results (see Figure 1.3). This radiation is emitted at an angle, θ , given by:

$$\cos \theta = \frac{\beta}{n} \quad (1.12)$$

This radiation is called Čerenkov radiation and can be used to identify charged particles.

Because of the energy of the expected incoming neutrino beam ($< 1\text{GeV}$) a water Čerenkov detector is all that's required [13].

The detector is divided into two separate chambers: an inner chamber and an outer chamber. The inner chamber is lined with 11,146 11-stage photomultiplier tubes (PMTs), each approximately 50cm in diameter. The tubes are placed at even intervals every 70cm covering 40.41% of the inner wall of the detector. Figure 1.4 gives an inside view of the detector and its wall of PMTs.

Behind the wall of PMTs on the inside chamber is a wall of black polyethylene terephthalate that is used to optically separate the inner chamber from the outer chamber. The outer chamber is also lined with outward facing PMTs which are

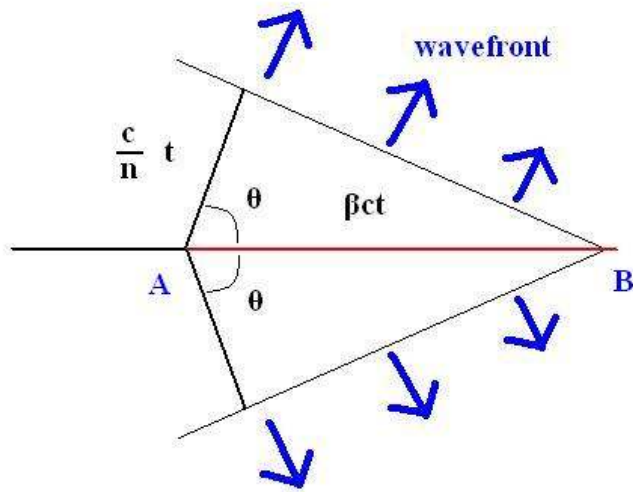


Figure 1.3: Čerenkov radiation: as the particle travels from A to B at a speed βc , electromagnetic radiation is given off at an angle, θ , determined by 1.12

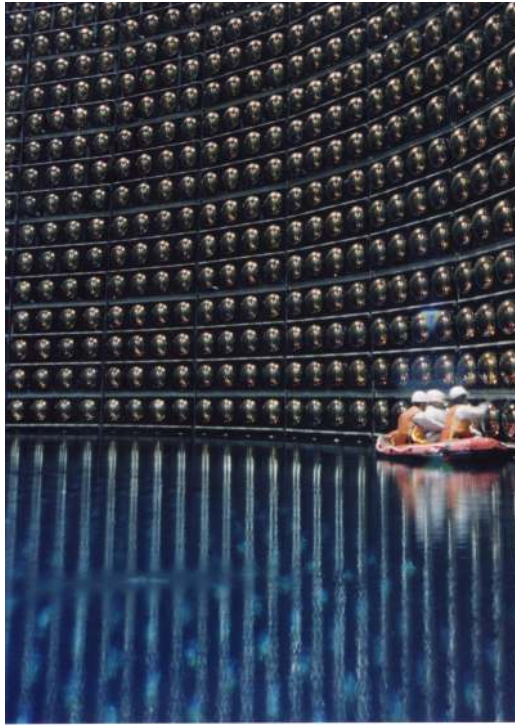


Figure 1.4: Inside view of SuperK and its 11 thousand PMTs. The boat and workers show the scale of the detector. [1]

used as “anticounters”. Each of these outer PMTs have a diameter of $\approx 20\text{cm}$ and are placed in such a way so that there are 2 behind every 12 inside PMT resulting in 1,857 outer chamber PMTs in total. Beyond the outer chamber is a second wall of highly reflective white polyethylene sheets to prevent as much outside interference as possible.

Because SuperK is housed underground, there is the possibility of radon contamination to deal with from decays in the surrounding rock. At the top of the detector, there is a 60cm gap between the top of the water and the top of the container where radon can build up which can then dissolve in the water, contaminating it. To handle this, radon free air is constantly pumped into the 60cm region to minimize contamination. If left unchecked, radon contamination can reach levels on the scale of $10 - 103\text{Bq}/\text{m}^3$. However, with the radon free air system, these levels are reduced to the order of $10 - 2\text{Bq}/\text{m}^3$.

1.2.4 Data Acquisition at SuperK

In order to collect data, SuperK has a sophisticated data acquisition system that relies on the use of a number of online (ie, those that run in real time with the experiment) and offline computers to handle the scores of data coming from the PMTs.

The signals from the PMTs are handled by a series of Analog Timing Modules (ATMs). There are a total of 934 ATMs and each one handles 12 different PMTs. The signal from the PMT is sent to the ATM which then triggers if the signal is greater than some threshold value (≈ 0.32 photoelectrons). If the trigger is met, then a rectangular pulse 200nsec long and 11mV high is generated (called a “HITSUM signal”). Each HITSUM signal is summed over and if it meets another trigger threshold of 320mV, the equivalent of about 29 hits (ie, 29 different PMTs must fire in a 200nsec window), then the signal is sent out to 8 online computers for data acquisition. The data from these computers is then sent to an online host computer which “accumulates” the data and sends it on in 70Mbyte “chunks” every 10 minutes to an offline offsite computer via fibre optics for later evaluation.

Currently, the threshold Čerenkov energies needed in order to stimulate the PMTs is $\approx 0.768\text{MeV}$ for electrons, 158.7MeV for muons and 209.7MeV for pions, but work is still underway to improve this triggering method through ongoing improvements to the water purification and data acquisition systems.

1.2.5 What to look for

Since Čerenkov radiation only results from charged particles traveling through the medium faster than the speed of light in that medium (and neutrinos are not charged particles), SuperK will be observing the resultant particles from neutrino charged current (CC) and neutral current (NC) interactions. That is, interactions involving an incoming neutrino, the exchange of a $W(+ \text{ or } -)$ or Z boson and result in a fast moving charged particle: a lepton in the case of CC interactions. See Figures 1.5 and 1.6.

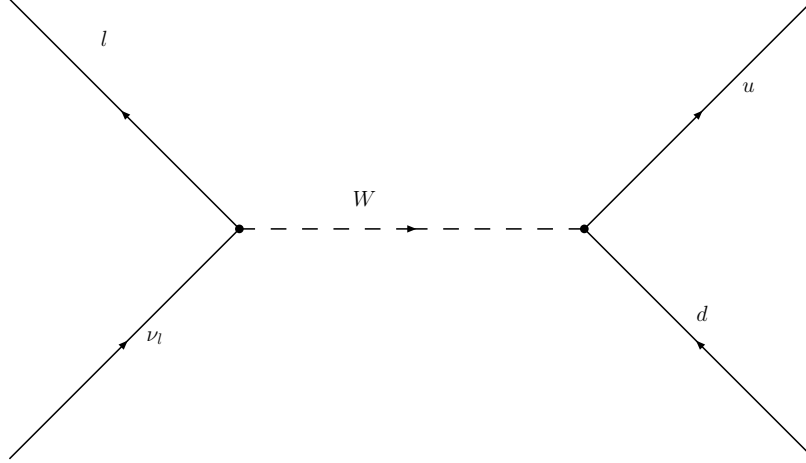


Figure 1.5: Sample Feynman diagram of neutrino weakly interacting with a down quark via (in this case) a W^+ boson resulting in the associated lepton (l) and an up quark, in this case turning a neutron into a proton. This is called a charged current interaction. Similar interactions are observed when a W^- boson would be exchanged, changing an up quark to a down quark (proton \rightarrow neutron). In this case, the direction of the W boson would be reversed.

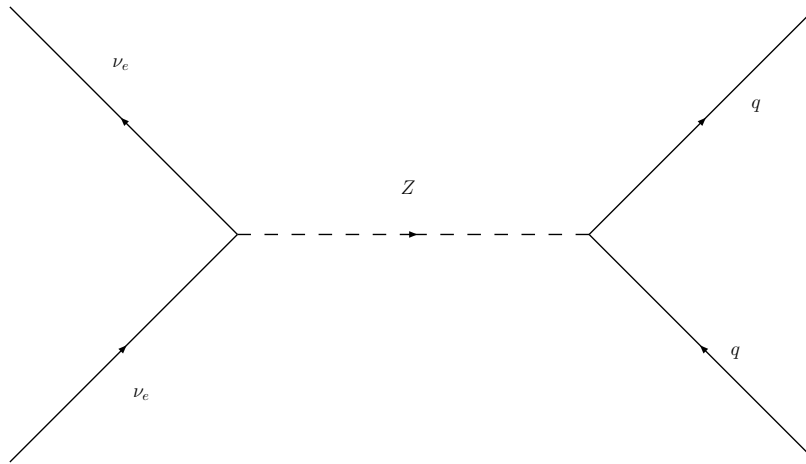


Figure 1.6: Sample Feynman diagram of neutrino weakly interacting via a Z boson. This is called a neutral current interaction.

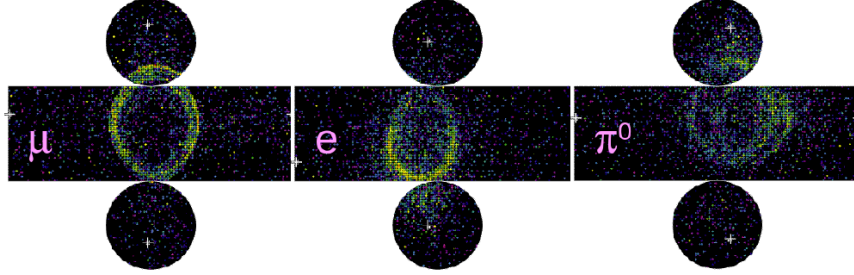


Figure 1.7: Image depicting how a muon, electron and π^0 events would be viewed by SuperK. While muon rings are clear, the photons from a $\pi^0 \rightarrow 2\gamma$ decay produces a fuzzy ring which can sometimes be mistaken for an electron.

Since neutrinos are electrically neutral, SuperK will observe the resultant lepton of the charged current interactions and, from this, determine which neutrino was involved. Distinguishing the lepton (and thereby determining what neutrino was detected) is done largely “by sight”. While a heavy muon will create a relatively “clean” signal, an electron will “bounce around” and create a “fuzzy” one (see Figure 1.7).

A problematic event occurs in the case when a neutrino scatters off a nucleus, resulting in a π^0 being created inside the nucleus. If this pion has the right energy, it can decay into two photons which, if theyre close enough together, can be mistaken for an electron which, in turn, can artificially inflate the electron neutrino measurements (see Figure 1.7). While this effect plays a roll in contributing error to the experiment, it is not expected to be enough to skew the results too much.

1.3 Beam Monitoring System

T2K employs a number of beam monitoring systems to check the beam and ensure its position and distribution are well monitored. If the beam is too wide, the horns won’t focus properly and part of the beam will be lost. If the beam is too narrow and intense it could result in damage to the target. If the proton beam does not hit the centre of the target, horn 1 won’t be able to focus the resultant pions properly (see Section 1.2.1). Because of 1.9, this can result in an improper neutrino beam energy which would greatly affect the results (see Section 1.1).

While there are a number of beam monitoring systems employed, the one that will be discussed here is the last one in place before the beam strikes the target: the OTR system.

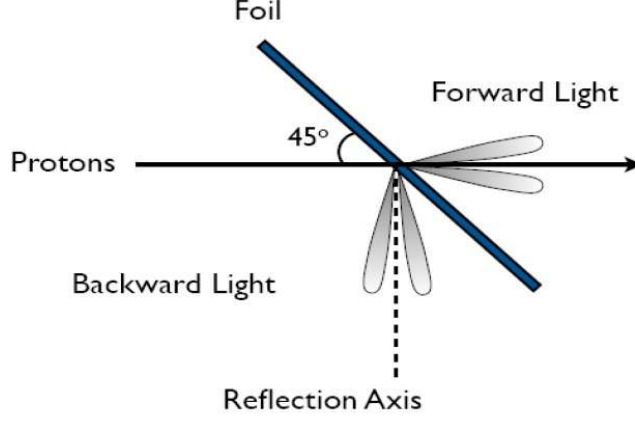


Figure 1.8: Illustration of the reflection of optical transition radiation as used in the OTR system. OTR is given off in a lobe like structure as determined by equation 1.13. This figure comes from [5].

1.3.1 Optical Transition Radiation System

OTR stands for Optical Transition Radiation. OTR is given off when a charged particle crosses the boundary from one medium to another with a different dielectric constant (a dielectric constant being an intrinsic property of a material). A moving charged particle has an electromagnetic field associated with it which is dependent on its surrounding medium and hence the medium's dielectric constant. When the particle crosses the boundary between two media, the fields have to reorganize themselves, resulting in part of the field being “shaken off” as optical transition radiation [12].

In the case of a proton beam passing through a foil, part of this OTR is emitted forward along the beam line and part is reflected back off the surface of the second material. If the foil is oriented at 90° to the incoming beam, the reflected TR will be reflected back along the beam line. However, if the foil is positioned 45° to the beam axis, the OTR will be reflected back at 90° to the beam path (see Figure 1.8). This OTR can then be used for beam monitoring purposes.

The photon yield, N , per unit solid angle, Ω , per unit photon frequency, ω , for the set up given in Figure 1.8 is given by

$$\frac{d^2 N}{d\Omega d\omega} = \frac{e^2}{\pi^2 c \hbar \omega} \left| \frac{\sqrt{\epsilon} - 1}{\sqrt{\epsilon} + 1} \right|^2 \frac{\theta^2}{\theta^2 + \gamma^{-2}} \quad (1.13)$$

where ϵ is the ratio of the reflectivity of the foil, θ is the angle between the emitted photons and the axis of reflection (NOT the angle at which it's emitted)

(see Figure 1.8), and γ is the relativistic gamma [16] [17]. For a 30GeV proton beam (what's expected at beam start up [15]), $\gamma = 32.3178336$.

Equation 1.13 is given in cgs (centimetre-gram-seconds) units, for which

$$\frac{e^2}{\hbar c} = \alpha \approx \frac{1}{137} \quad (1.14)$$

where α is the fine structure constant. Looking at only the visible spectrum of light (ie, photons of wavelength $\approx 400\text{-}700\text{nm}$), equation 1.13 becomes

$$\frac{dN}{d\Omega} = \frac{\alpha}{\pi^2} \left| \frac{\sqrt{\epsilon} - 1}{\sqrt{\epsilon} + 1} \right|^2 \frac{\theta^2}{\theta^2 + \gamma^{-2}} \ln \frac{7}{4} \quad (1.15)$$

It's important to note that the OTR is not given off in a single direction but in the lobe like distribution in Figure 1.8. No OTR is given off along the axis of reflection ($\theta = 0$) as is evident from both the figure and equation 1.13.

The OTR team will utilize the concept of optical transition radiation to monitor the proton beam.

1.3.2 OTR system design

In order to monitor the beam, the OTR group uses a thin piece of titanium foil inserted into the beamline at a 45° angle. The OTR is then reflected off of a series of 4 rad-hard, parabolic mirrors to a rad-hard camera. Because of the high radiation expected near the beam ($8 \times 10^3 \text{Gy/h}$ at mirror 1), conventional devices cannot be used to look at the OTR directly and hence the OTR must be transmitted out of the higher radiation areas to a mounted camera outside the beam enclosure. Figure 1.9 shows the relative set up of the entire system. Figure 1.10 shows how the beam profile as viewed from the OTR compares to the actual beam profile.

The first three mirrors have a focal length of 110cm while mirror 4's focal length is 60cm . The camera used in the system is affixed with a fibre taper to help rescale the image down to the chip size. The camera is discussed in more detail in Chapter 2 while the fibre taper is briefly discussed in Section 2.1.

The OTR system uses a number of foils and a mechanical arm affixed with a disk to rotate between them. The disk and foils are both made of titanium. The motor is mounted on the horn some metres away from the actual disk. Rotations will be facilitated by a long shaft with flexible components. This introduces a potential source of slippage for the motor but is necessary to keep the motor away from the higher radiation zone directly around the beam. The motor controls and disk rotation are discussed in greater detail in Chapter 3.

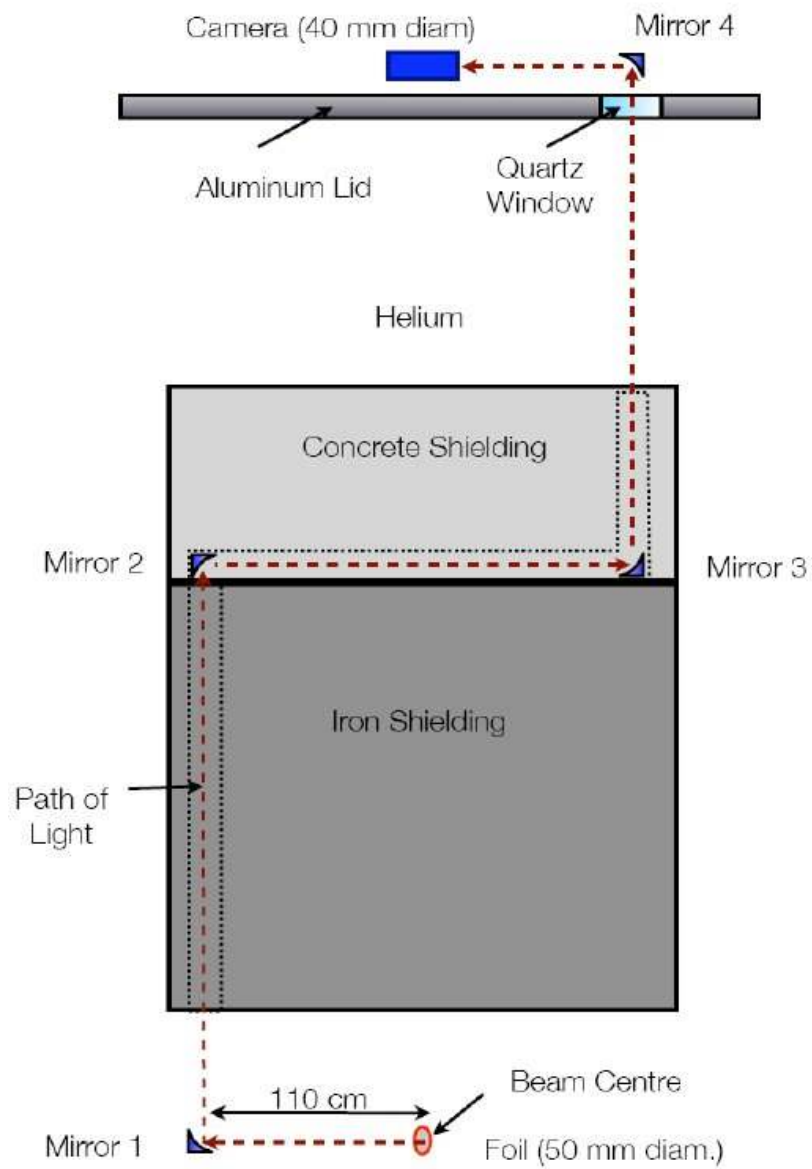


Figure 1.9: Set up of the OTR system mirrors. The beam, here, is heading into the page. [5]

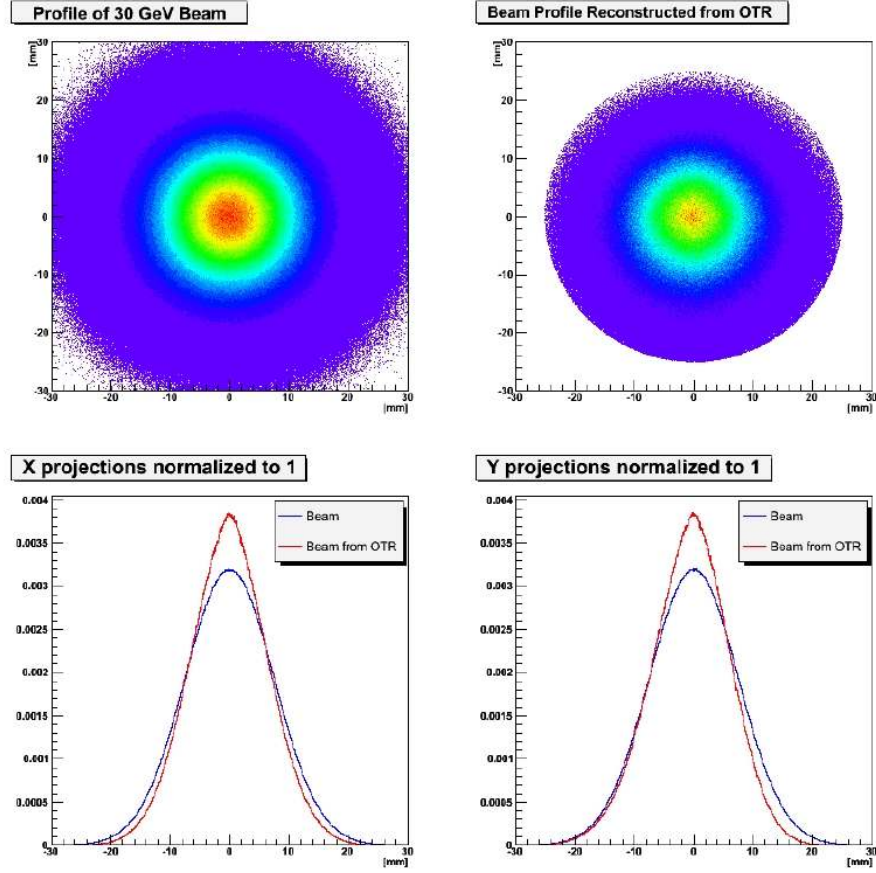


Figure 1.10: Top left is a simulation of an “actual” 30GeV Gaussian beam while top right illustrates how this same beam would appear through the OTR system. The lower graphs illustrate how the beam profile from OTR will compare to the actual beam profile. Image provided by [11].

Chapter 2

Camera Gain

“Gain”, when talking about digital cameras, is a specific quantity that relates the number of electrons per pixel to the count the pixel gives (the measure of “brightness”). The camera gain relates the output count of the pixel (what is stored in an image) to the actual number of electrons produced in the camera by incident photons per pixel. As more electrons are read, a higher count is given to indicate a “brighter” spot on the camera. At the lowest values, the pixel count isn’t quite zero due to intrinsic characteristics of the background of the camera. This non-zero background is known as the “pedestal” of the camera. Eventually the pixel count caps out at the saturation point, but before then it increases in a continuous and predictable fashion. This relation is called the “gain curve”.

Not knowing the gain curve can have adverse effects for beam monitoring. The proton beam (and hence the OTR off of the foil) is not flat but appears in some distribution with the greatest intensity in the centre and some calculable “die off” as it goes to the edges; this is called the “beam profile” (see Figure 1.10). If the beam is too intense at the centre compared to the outsides there is risk of damaging the target and thus affecting data gathered later on. Further, if the beam is too broad, the first horn will be unable to focus all the secondary particles and parts of the beam will be lost. Without knowing the gain curve precisely, it would be impossible to determine the actual beam profile from what is captured by the camera.

In order to study the gain curve of the camera a series of images were taken at varying light levels and the results plotted.

2.1 Camera

The camera used by the OTR system is a 768×475 displayed pixels¹, 8-bit Thermo Scientific Charge Injection Device (CID) 8710D1M MegaRAD camera. Pixel dimensions are $12.0\mu m \times 13.7\mu m$. Pixel readout is as a signed character

¹Because of the framegrabber board used, images are read out with 692×480 pixels.

(value between -128 and 127). A fibre taper, which reduces the image by a factor of 3.6, is attached to the front of the camera to allow it to read images which are larger than the physical dimensions of the chip.

Charge Coupled Device (CCD) cameras are more common in the market, but are more prone to degradation in high radiation environments. A CID was chosen because it is less susceptible to radiation damage (rad-hard) and can handle the radiation in the region it would be mounted, which is about 70 mGy/h [17]. A rad-hard CID can survive upwards to 1×10^4 Gy, compared to a CCD which can only survive a total dose of about 2×10^2 Gy².

While it was expected that the camera’s gain curve would be linear, tests were done to find how linear and in what regions such an approximation would be valid. Since the beam profile is non-uniform, any non-linearity in camera gain could lead to an inaccurate perception of beam intensity over the profile. Ultimately, any non-linearity in the gain curve would need to be corrected for elsewhere in the system, either during or after image capture. A linear gain curve, alternatively, means that no such correction would need to be made. The less that needs to be corrected for, the greater the ease of data collection and less need for approximations and hence less room for error.

2.1.1 Camera Pedestal

Before analyzing the gain curve it was first necessary to look at the pedestal of the camera. The pedestal serves as the “zero brightness” level of a camera and gives an idea when the camera no longer can “see” incident photons. To get the pedestal a series of images were taken with the camera in a dark place.

A series of ten images were taken and averaged to give the pedestal of the camera. These results were then output in the form of a profile showing the distribution of the pedestal over the camera’s chip. A colour scale was chosen to make the contrast clearer (see Figure 2.1).

The pedestal is averaged at 10.6 (out of 255) over the entire camera with significantly higher background around the left corners and far right middle. There is also a noticeable line of cut off at about 80 pixels from the left. This was speculated to be the result of the camera chip being fashioned out of two separate parts. It has also been speculated (by the manufacturer) that the high pedestal values around the edge are a consequence of how the fibre taper was glued to the chip.

2.2 Finding the Gain Curve

Using a series of neutral density filters a series of pictures were taken using the camera to measure the camera response at varying levels of light. A neutral density filter is a shaded piece of transparent material (usually glass) that can be used to reduce the amount of light transmitted from a source. Each neutral density filter has an optical density (OD) associated with it. From the OD

²According to manufacturer.

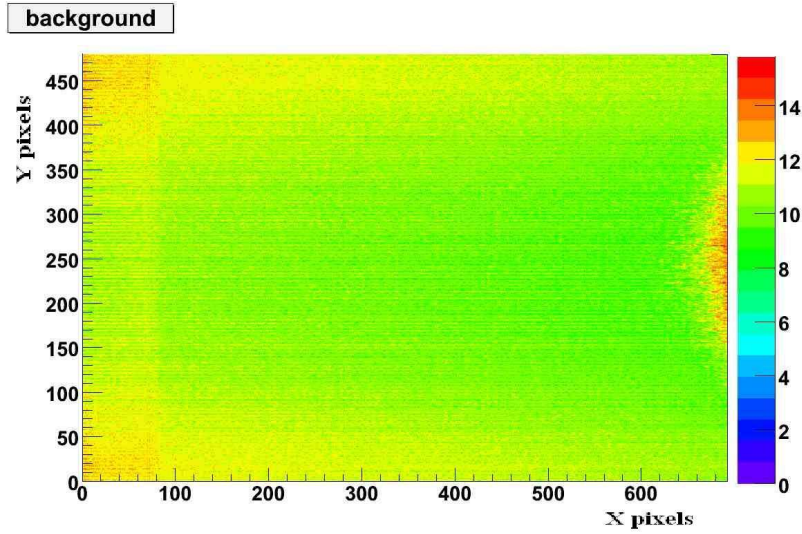


Figure 2.1: Background of Thermo Scientific CID8710D1M MegaRAD camera + fibre taper. Fibre taper is described briefly in Section 2.1.

value, light transmission can be easily calculated. For example, an OD of 0.3 corresponds to a light transmission of roughly 50% (see equation 2.1). That is, the light source is reduced by a factor of 50%. For efficiency, only filters of OD 0.05, 0.1, 0.2, 0.3, 0.7, 1.0, 2.0 and 3.0 were used in various combinations to completely sweep the range from saturation (no filter) to essentially pedestal. This sweep was done first in increments of 0.10 from 0 (no filters) to OD1.0 and in increments of 0.05 from OD1.0 to OD3.0.

An ideal neutral density filter would reduce ALL wavelengths of light evenly. However, in practice, neutral density filters of different OD values will filter different wavelengths of light very differently. To account for this, a laser light source was used. Because the filters were calibrated with a 546nm light source, a green laser was preferred. To ensure a diffused, uniform coverage over the entire face of the camera, a make-shift integrating sphere was also used. For a diagram of the set up, see Figure 2.2.

$$transmission = 10^{-OD} \quad (2.1)$$

An integrating sphere works by taking a single light source (in this case, the laser) and through a series of internal reflections off of a reflective medium (white paint), emits a flat-diffused light out of an emission hole cut in the side (see Figure 2.3). The laser is aimed toward the centre of the sphere with the camera itself being placed nearby a few centimetres from the diffused light source.

Once the filters, camera and light source were in place, a series of grey-scale images were taken, 10 per each OD level. For a sample of what was looked at,

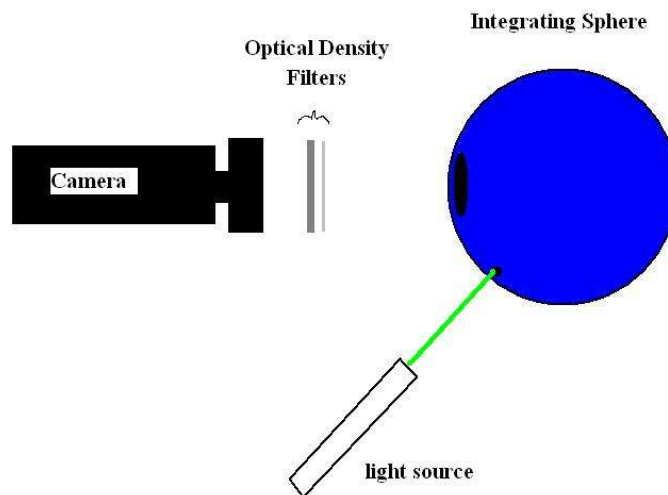


Figure 2.2: Basic diagram of set up used for testing camera gain. Camera, light source and integrating sphere were kept stationary throughout testing while neutral density filters were swapped in.

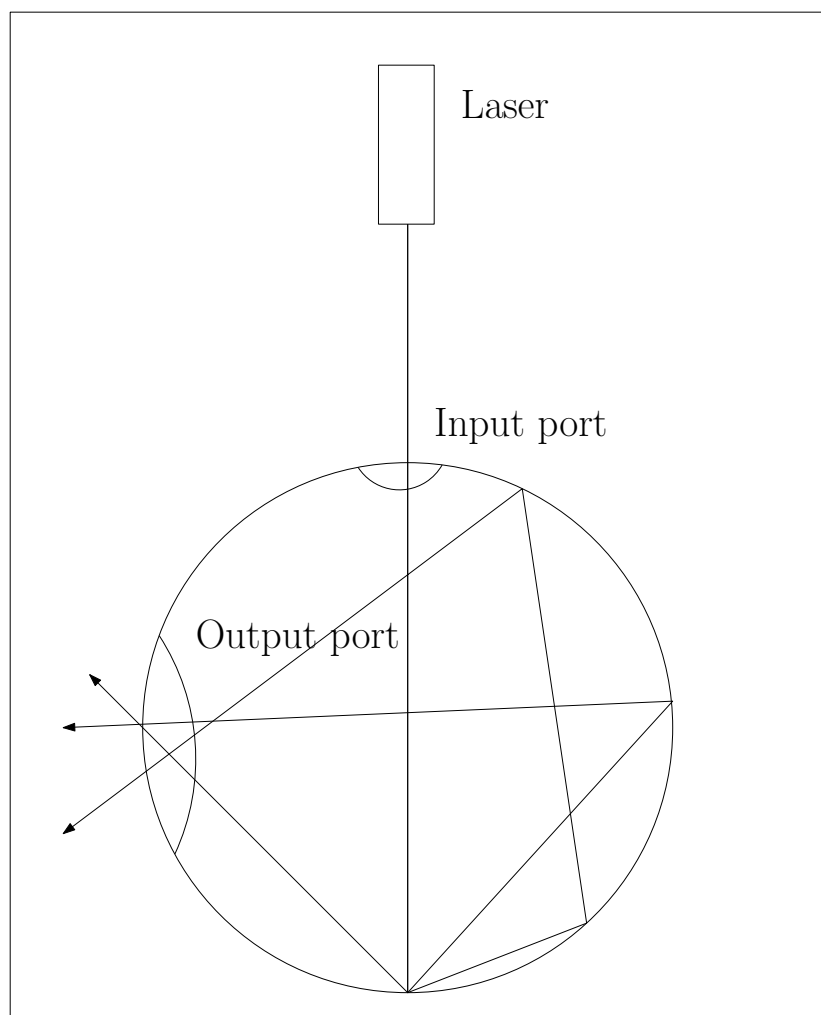


Figure 2.3: Diagram illustrating basics of how an integrating sphere works.

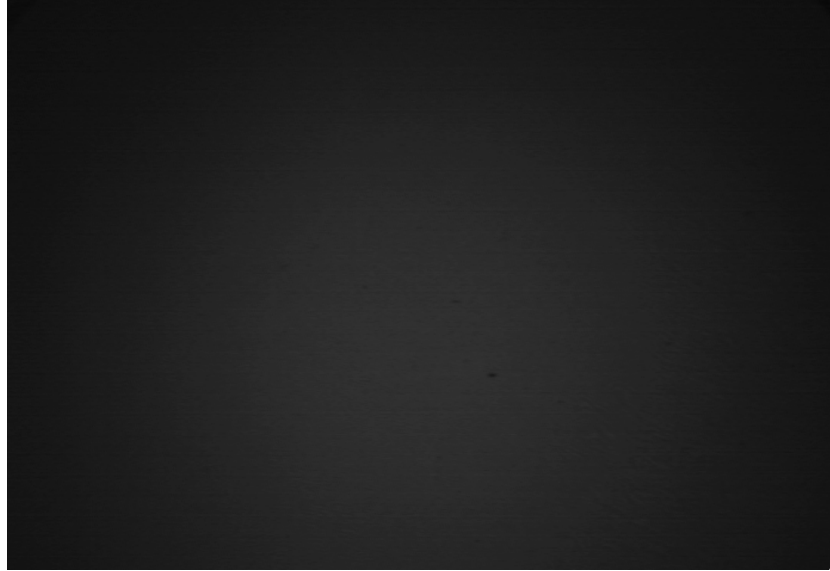


Figure 2.4: Sample grey-scale image from gain tests. OD1.0.

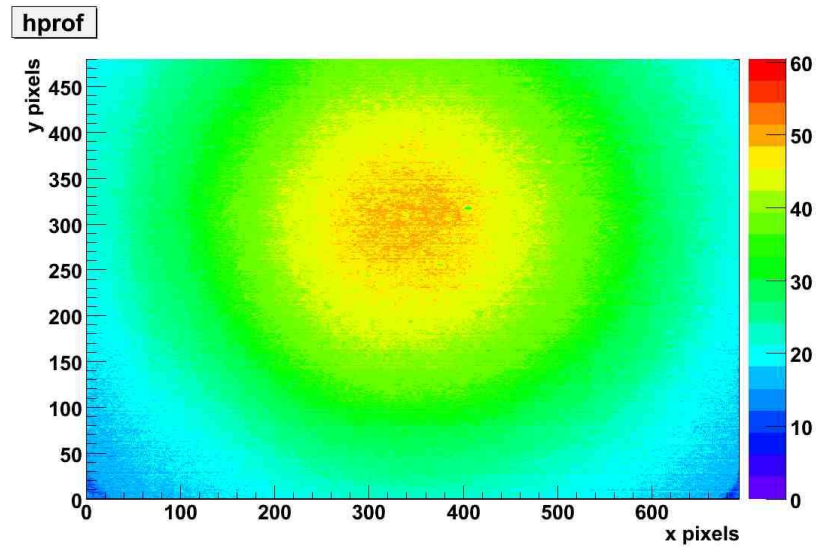


Figure 2.5: Sample image above, displayed here with a colour map. The non-uniformity of the image is a result of the fibre taper. Note: this image is upside-down relative to the one above.

see Figure 2.4 and Figure 2.5. It is important to note that the non-uniformity observed in these images is a result of spatial variation in the light transmission of the fibre taper and not a result of the light source. Essentially, the more curved fibres around the edge of the taper have greater light loss than the straighter fibres nearer to the centre. This is being corrected for elsewhere in the system and is not a matter to be discussed here.

2.2.1 Analysis

To find the gain curve, the grey-scale images taken by the camera were input into ROOT (An Object Oriented Data Analysis Framework³) and each OD level's 10 images were averaged. Graphs were created for each pixel individually, mapping pixel count to the light transmission levels (given by 2.1). The error on the neutral density filters were given by the manufacturer to be 4% of the given OD value. This translates to an error on the actual light transmission as given by equation 2.2 where ΔOD is the error on the OD of the filter (4% as above).

$$\Delta trans = 10^{-OD} * \ln(10) * \Delta OD \quad (2.2)$$

According to OD curves supplied by the manufacturer comparing wavelength to OD, the OD2.0 filter acted more like an OD1.94 filter within the desired range. Although this was within the stated 4% error bounds given by the manufacturer, it was far enough off of the stated OD to require a correcting factor of 0.06 to be taken off the stated OD level of the filter during analysis.

Once the correcting factor was input, the graphs were fitted to a line and the slopes, intercepts and reduced chi squares (measure of how “good” a fit is) for each pixel were recorded. Figures 2.6 and 2.7 give an example of the fit curves and data for a single pixel on the middle of the chip. Linear fits were taken over a region of 15-200 in pixel count (x-axis).

Overall, the fits were very good with most reduced chi squares being well below 1 (Figure 2.8). While the chi squared of the corner pixels did come out significantly off, this was a result of a combination of the fiber taper (as discussed before) and the broad fit range specified and not a characteristic worth noting. It is, however, noteworthy that a level off in pixel count occurs in the lower light regions 1 to 2 counts from the pixel's pedestal value. This means that within 1 or 2 counts of pedestal (roughly 1% of light transmission, according to Figure 2.7), the pixels will appear slightly brighter than they should be. Further, the x-intercept for the fit is much lower than pedestal for this pixel (6 compared to 12) which means that the camera is reading “zero light” before the actual zero light levels. Unfortunately, there is nothing that can be done to correct for this.

³See ROOT homepage: <http://root.cern.ch/>

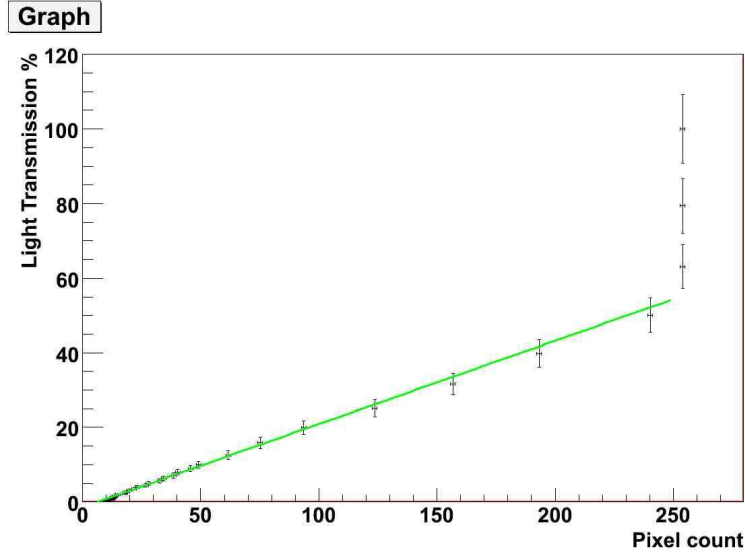


Figure 2.6: Plot showing pixel count (out of 255) vs light transmission (%) for middle pixel on chip. Fit is over the region 15 to 200 in pixel count. Reduced chi square for this fit is 0.312. Saturation was reached at about 50% light transmission.

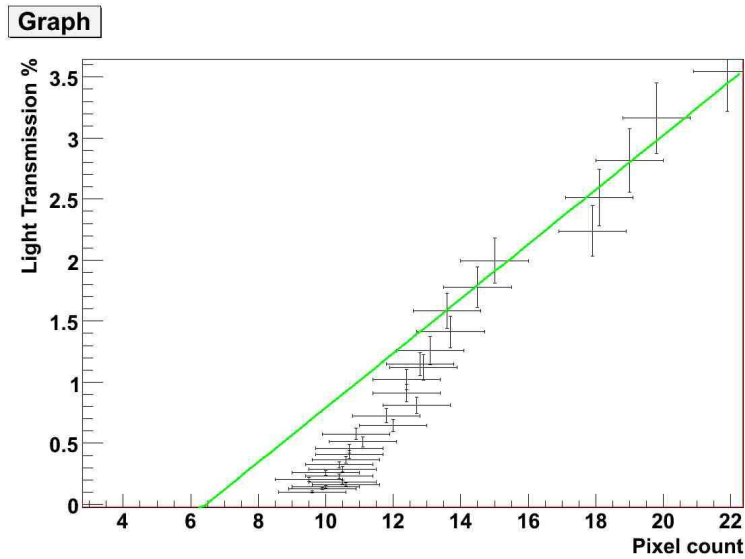


Figure 2.7: Zoom in of lower region of Figure 2.6. There is a noticeable level off in pixel count one to two counts from pedestal (10, in this region).

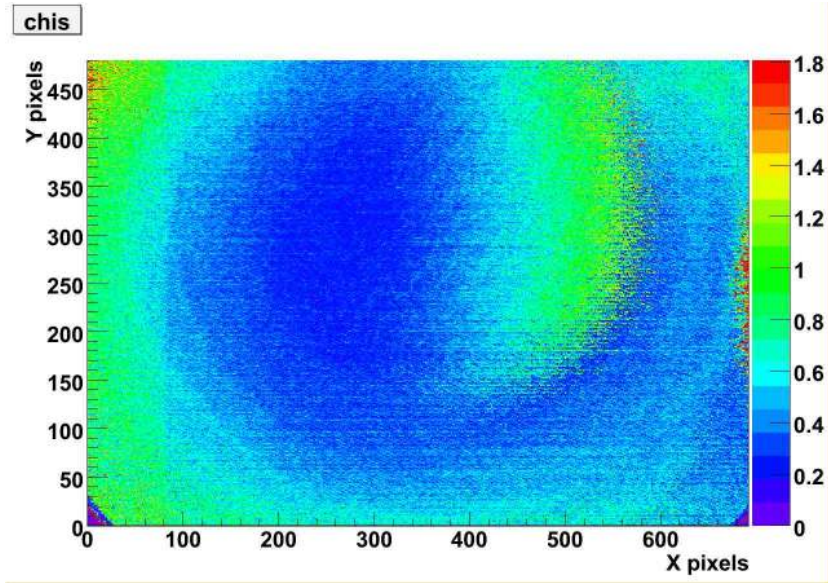


Figure 2.8: Map of reduced chi squares of linear fit for each pixel on chip. The lower corners of the image are off due to effects of the glued on fibre taper. These effects were briefly noted in Section 2.2.

2.3 Camera 2

To make sure the level off in pixel count noticed in Figure 2.7 is a characteristic of the camera and not a consequence of an error in the analysis, another series of images were taken using a second camera. This time the tests were done using a red laser light source (due to lack of availability of a green laser at the time). The camera used this time was a 768×493 displayed pixels⁴, 8-bit Pulnix TM-t45E CCD (Charge Coupled Device) with pixel dimensions $11.0\mu m \times 13\mu m$. There was no fibre taper attached to this camera.

2.3.1 Analysis of Camera 2

The analysis of the CCD camera was carried out in the same manner as for the CID camera + fibre taper, except for the use of a red laser. A series of grey-scale images were taken and input into ROOT and linear fits were made for each pixel. Figures 2.9 and 2.10 give an example of the linear fit and data for the middle pixel on the CCD chip. The fit range used was from 25-200 in pixel count. This fit range was used due to the different pedestal values for the CCD and CID cameras. The pedestal for the CCD camera was found using the approach described in Section 2.1.1.

⁴Again, due to the framegrabber, readout pixels are different from active pixels.

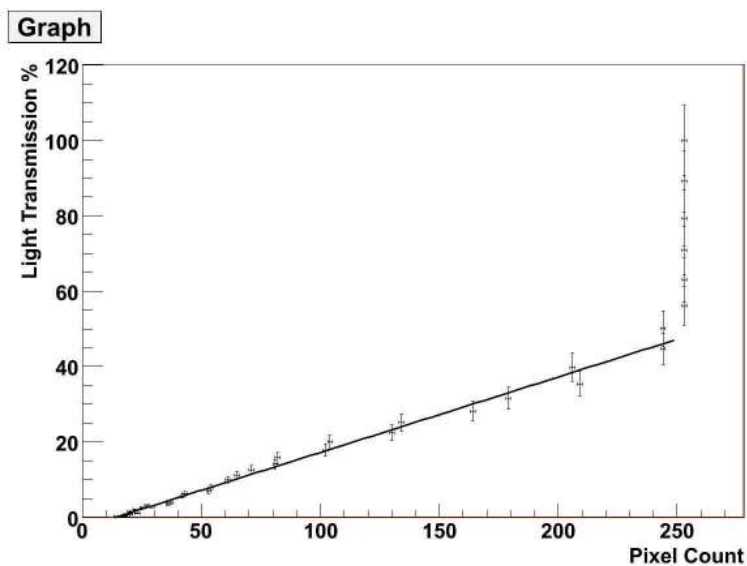


Figure 2.9: Plot showing pixel count (out of 255) vs light transmission (out of 100) for middle pixel of the CCD camera. Fit is over the region 25 to 200 in pixel count. Reduced chi square is 1.39. Saturation was achieved at about 50% light transmission.

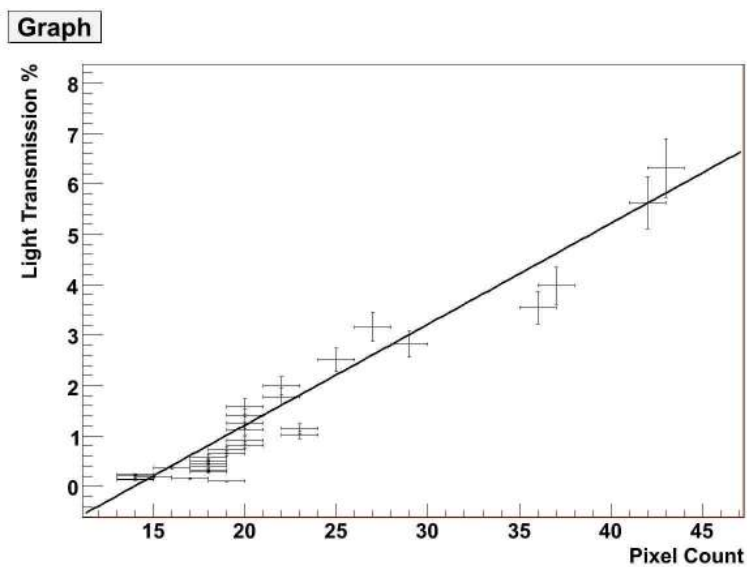


Figure 2.10: Zoom in of lower region of Figure 2.9. Linear fit appears to go straight to origin with an x-intercept closer to pedestal value than for the CID. Pedestal for this particular pixel is 15.

While there seemed to be some kind of level off near pedestal, the use of the red laser, for which the filters were not calibrated, and the lack of correction factors for some of the filters⁵ resulted in some scatter about the line and a worse chi square as shown in Figures 2.9 and 2.10. Generally, however, the fit is linear to the intercept. The intercept is also far closer to the actual pedestal for the middle pixel (both around 15) than was the case for the CID camera (see Section 2.2.1), suggesting that the level off noticed in Figure 2.7 is an intrinsic characteristic of the CID camera and not the consequence of an error in the analysis.

2.4 Additional Work on Camera Gain

While camera analysis is not often a topic for neutrino experiments, it is in other fields⁶. As such, there exists papers that talk at great length about gain curves for various camera chip types, but often as a function of exposure time, not light level. Even so, it has been corroborated by others that the level off of the CID camera [3] noticed in Figure 2.6 and the near completely linear response of the CCD camera [4] are intrinsic characteristics of CID and CCDs respectively.

2.5 Gain Corrections

Since the gain curve of the CID camera + fibre taper is largely linear, there is no need to correct for it within the OTR system. The level off in the lower light region of the CID may result in loss of image quality at low light, but since it only occurs within 1 or 2 counts of pedestal, it will be of little concern.

While the camera reaching pedestal before actual zero light levels may be problematic, it is a characteristic of CID cameras and no correction is possible. Since CCD cameras are not sufficiently rad-hard, an alternative camera is not a viable option and the system will just have to deal with this.

As far as gain correction is concerned, none has been included in the OTR system as of this time.

⁵OD0.7 and OD0.3 behave more like OD0.75 and OD0.35 filters in the red light region.

⁶astronomy or photography

Chapter 3

Motor Controls

The OTR motors system is used for two primary purposes: to move the camera on an XYZ stage and to rotate between the 8 foil positions. Since both the camera and the foil disk are located in high radiation areas, the disk being in the beam line, it is necessary to have some automated control over these processes. To accomplish this, motor controller software and a user friendly GUI were written utilizing MIDAS, a data acquisition system written by TRIUMF and PSI¹, to send commands directly to the motors².

Due to the accuracy required of the OTR system, it was necessary to test the motors for precision in movement, particularly the arm motor, the motor responsible for rotating foils, as rotations must be accurate to within less than a millimetre. To do this, a series of tests were run with the arm motor using different movement methods, measuring the accuracy of each move.

3.1 Motors

The motors used in the OTR system are a series of Velmex PK245-01BA 2-phase stepping motors. Each motor has 200 steps and 64 micro-steps with a step accuracy of 0.05° .

The motors are connected to a nearby computer through a private Ethernet network. Commands are issued by a MIDAS front end to a motor controller box that relays the commands to the individual motors.

The stage motors were attached to a screw with a stage. Each screw had an advance of 1 mm per turn. The X and Z stage motors have a total sweep of 4" left to right and back to front whereas the Y motor has a sweep of 2" top to bottom. Each motor includes a limit switch - a button located at either end that informs the motor controller when the stage has reached its limit.

¹See MIDAS website: <https://ladd00.triumf.ca/~daqweb/doc/midas/html/index.html>

²See Appendix A for the basic framework used by the GUI.

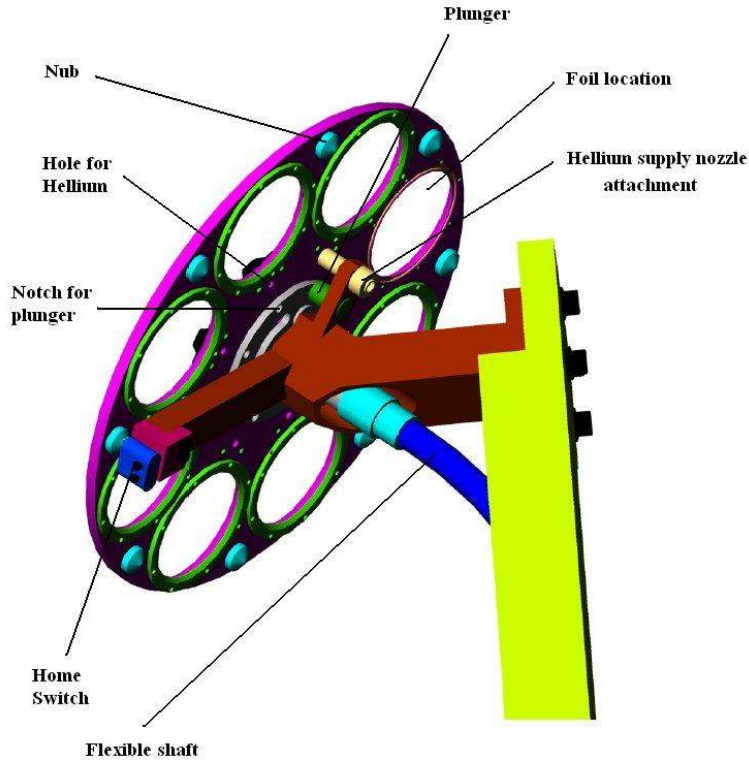


Figure 3.1: Labeled diagram of disk + arm, outlining the location of key components. [5] [17]

3.1.1 Arm Motor

The arm motor was equipped to handle a number of different methods of motion. The first method of motion was a standard fixed degree rotation specified by the user. However, as back up systems, two other forms of motion were enabled: limit home motion and pressure home motion.

Limit home, or “home” commands allow the motor to rotate until a limit switch is pressed, stopping the motion. This switch is attached to the arm while a series of 8 metal nubs are attached to the disk. When the switch moves over the nub, the nub closes the switch, stopping the motion (see Figure 3.1).

For pressure home, or “phome” commands, a helium feed is ran down the arm to the disk. As the disk rotates, the helium supply is blocked by the disk until it reaches one of the foil positions where a small hole allows the helium to flow freely through (Figure 3.1). A pressure sensor is situated near the motor that reads the pressure of the helium, stopping the motion when the pressure

drops below a user-set threshold pressure.

To ensure accuracy of the motion systems, there is a spring loaded plunger that pushes a ball into notches on the back of the disk located at each foil position (Figure 3.1). The plunger is designed to lock the disk into place when the foil is in position.

While the disk itself will be located in the beamline, the arm motor will not be, necessitating a long shaft, parts of which are composed of flexible units to allow a small degree of bending. The shaft will allow the motor to rotate the disk from a ways away. While necessary, this does introduce another degree of error in the motion in the rotation of the disk.

3.2 Motor Motion

To analyze the arm motors motion, a metric-2 hole, 85mm from disk centre was used as a fixed point on the disk and a light source was placed on one side with a camera on the other. As the disk completed a full rotation, an image was captured. Ten images were taken for each motor motion, both with the plunger and without. Images were analyzed to quantify the disk drift over time. A sample image is shown in Figure 3.2.

The camera used for these tests was a CommandShot SMX-160C 6.6 megapixel (2208×3000) CMOS USB camera. Each pixel has a physical dimension of $3.5\mu m \times 3.5\mu m$. The aspect ratio used for the images was 1:3 which results in a readout grid of 736×1000 pixels.

3.2.1 Fixed Rotation

Fixed rotations only require the user to enter a degree amount and order the motor to rotate. The motor will then rotate the given number of degrees until it reaches its destination, according to the motor. Problems with this method of motion can arise due to disk slippage in the shaft or at the motors end. The motor will always rotate what it thinks is the correct amount (within its own error of 0.05° per step), but the actual degree of rotation can vary due to the presence of the shaft.

In analyzing the effects of the “rotate” command, profiles of the images were plotted for a visual display of the disk drift. Using only the “rotate” command, the disk drift was seen to be about 15 readout pixels or about $156\mu m$ as seen in Figure 3.3 with the plunger compared to $1575\mu m$ as seen in Figure 3.4 without the plunger. The large drift without the plunger is likely due to rotational motion being absorbed in the flexible parts of the shaft.

3.2.2 Home Switch

The home switch works by allowing the motor to rotate so long as the home switch is not closed. The user issues the “home” command and the motor is allowed to rotate until the home switch is closed once more. While at each



Figure 3.2: Sample image. A metric-2 hole, 85 mm from disk centre with back-lighting. The aspect ratio used is 1:3.

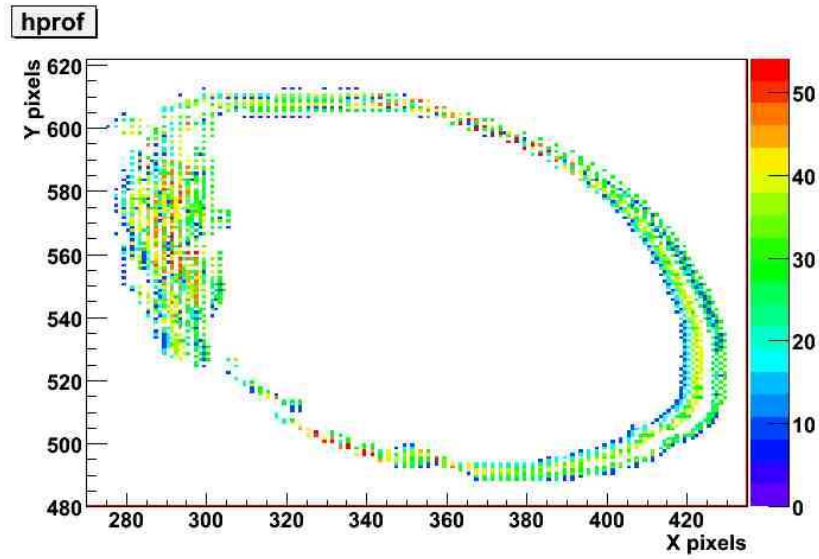


Figure 3.3: Visual display of drift from “rotate” command with plunger in place. The acceleration of the motor was set to 5 revolutions per second squared. The different colours here signify different runs.

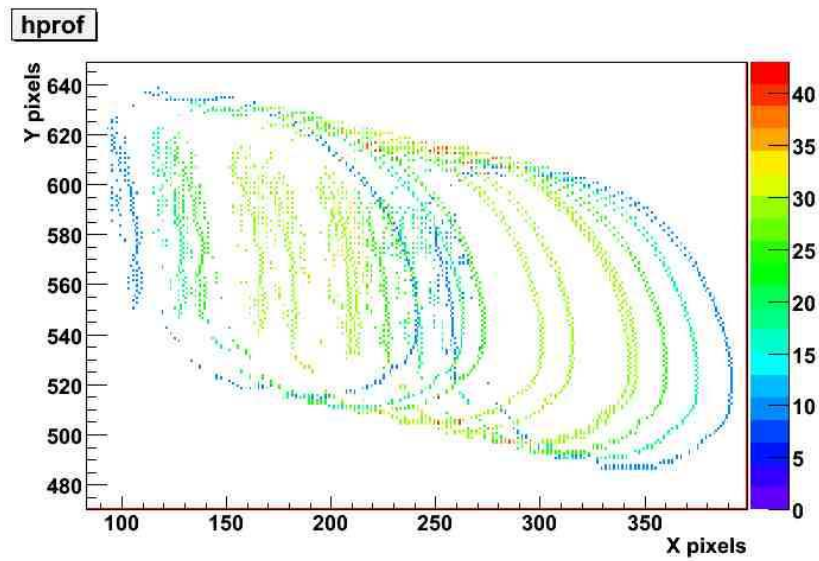


Figure 3.4: Rotate command without plunger. The acceleration of the motor was set to 5 revolutions per second squared.

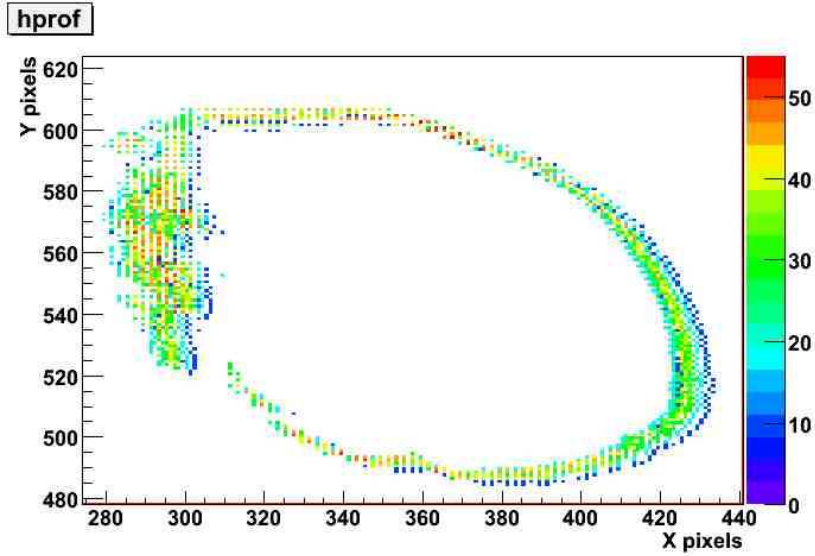


Figure 3.5: Profiles of hole for ten rotations using only the Home command with the plunger in place. The acceleration of the motor was set to 5rev/s^2 .

foil position there is a nub that serves to close the home switch, turning it on and stopping the motion, the switch is left open between foil positions allowing the motor to rotate freely. There is a delay required by the motor before an activated home switch is acted upon. This allows the motor to start rotating even if the home switch is already on. One of the dangers of the home switch method to be wary of is that if the speed of rotation of the motor is set too high, the disk can travel over a given nub before the delay is up, thereby allowing the disk to continuously rotate. Because of this, the arm motor has to be set to a slow but steady pace for the greatest degree of accuracy, but ideally also a fast deceleration to allow the delay a chance to expire when the switch is closed by a nub.

As far as accuracy is concerned, using only the “Home” command with the plunger, the disk drift is comparable to the rotate command with a total drift of about $156\mu\text{m}$ (see Figure 3.5). However, without the plunger it performed almost as badly as the rotate command did with a disk drift of about $1155\mu\text{m}$ (see Figure 3.6). As with the rotate command, the plunger is necessary to ensure the disk arrives at the proper foil location.

3.2.3 Pressure Sensor

The pressure sensor system works similarly to the home switch command. A helium feed is aimed at the disk. While normally the disk will block the helium flow, resulting in the pressure sensor reading a higher pressure, holes in the disk

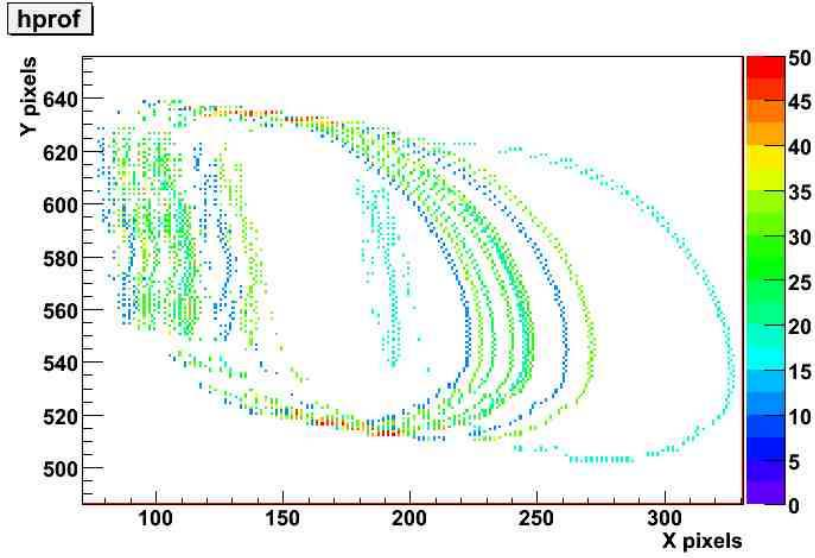


Figure 3.6: Profiles of ten rotations using home command without plunger. The acceleration of the motor was set to 5rev/s^2 .

at each foil location allow the helium to pass through and lower the pressure. The “Phome” command is issued by the user and the motor is allowed to rotate. The motor continues to rotate until the pressure drops below a user specified threshold. This threshold pressure must be specified *before* the motion begins and cannot be changed during. Again, a delay is necessary to allow the motor to begin motion from a lower pressure position.

Again, comparing the Phome command with and without the plunger, it becomes apparent that the plunger is playing a central role in reducing disk drift. With the plunger, the disk drift was less than $525\mu\text{m}$ (as in Figure 3.7) compared to more than $1890\mu\text{m}$ without.

3.3 Conclusions

From all the runs, it is clear that the most important factor in reducing disk drift is the presence of the plunger. The devastatingly large drift noticed in the lack of plunger tests is likely due to disk slippage during the rotation. The plunger, in effect, corrects for this by forcing the disk into the proper position once it’s completed its rotation.

While it is hoped that the plunger does not break, the degree of accuracy required by the OTR system cannot be guaranteed without it. Though the home switch and pressure sensor motion methods are only intended as back up systems, their inaccuracy without the plunger is still a worrying matter of consideration. These results are summarized in Table 3.1.

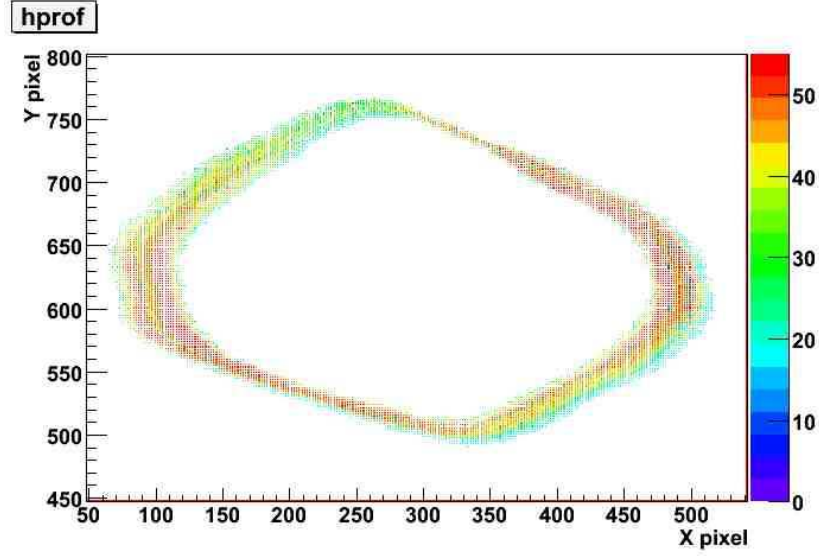


Figure 3.7: Profiles of hole for ten rotations using only the pressure sensor and Phome command with the plunger in place. The acceleration of the motor was set to $2\text{rev}/s^2$. The pressure threshold used during these runs was 33.1 PSI with a max/min pressure reached of 67.5/27.7 PSI.

	Fixed Rotation	Home Switch	Pressure Sensor
Plunger	156	156	525
No Plunger	1575	1155	1890

Table 3.1: Table comparing disk drift (in μm) of each method with and without the plunger in place.

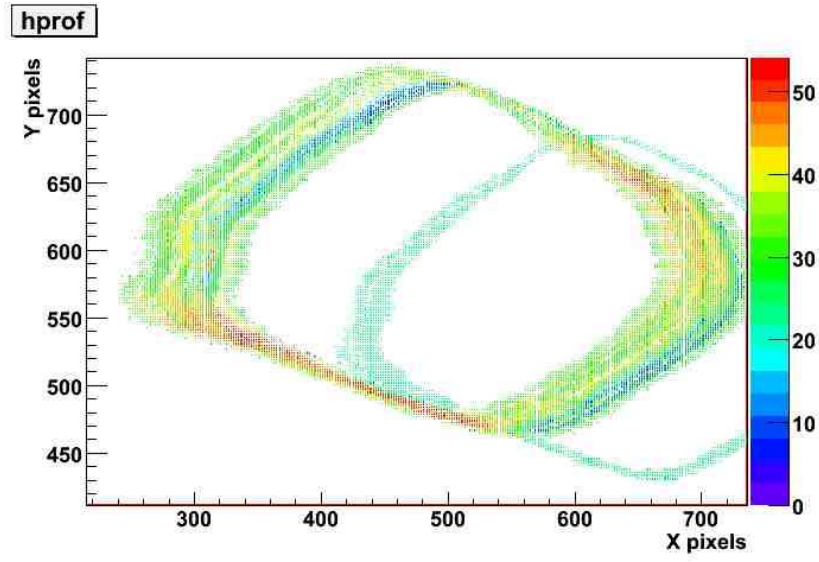


Figure 3.8: Profiles of ten rotations using Phome command without plunger. The image is cut off at the side due to disk drift exceeding visual range of the camera. The acceleration of the motor was set to $2rev/s^2$. The pressure threshold used during these runs was 32.2 PSI with a max/min pressure reached of 87.4/23.1 PSI.

In the result of a rotation failure, either due to the failure of the plunger or another system, it is foreseeable that the disk itself would become stuck in the beam path. While a thin piece ($50\mu m$) of titanium foil is unlikely to cause much damage to the graphite target, that may not be the case for the much thicker titanium disk that houses the foil. One of the problems the OTR team had to anticipate is what to do if the disk were to become stuck in the beam path and what potential damage would result to the target. To this ends, simulations were done to evaluate the potential damage to the target and are discussed in Chapter 4..

Chapter 4

Simulations in Fluka

Starting in November 2007, a series of simulations were run to test the effects of the OTR arm getting stuck and blocking the proton beam. These simulations were conducted largely in fluka (version 2006.3), a Monte Carlo simulation package, to evaluate what secondary particles would be created in the event that the OTR arm were to get stuck in the beam's path. These simulations were later extended to see what affects these secondary particles would have (in terms of radiation dose) on the fixed target located 30cm away. This was done to see if it would be necessary to include a feature that would allow for the disk arm to drop away should it get stuck in the beam path. While the simulations themselves were run in fluka, the results were later evaluated using ROOT.

A geometry was specified using the format required by the fluka input card¹. The OTR arm was approximated by a 0.7cm titanium disk with an 11.25cm radius and was oriented 45° from the incident beam axis. A second object, a 2cm thick, 57 × 52cm² aluminum target, was also specified and placed 30cm downstream of the off axis OTR arm (see Figure 4.1). A beam of 25,000 40GeV protons was then specified and a series of simulations were run.

The first part of the simulation was to see what secondary particles were created. For this, the aluminum target was omitted and just the particles that crossed a boundary 30cm from the OTR arm were looked at (ie. particles that were deflected back and those that were scattered off at high angles were omitted from the results). For the second part of the simulation, the aluminum target was included and radiation dosage to the target itself was examined.

4.1 Evaluation

Using ROOT, a histogram was created using the incident particles energy on the z-axis and the cross section facing the beam on the x and y-axes to show where the largest amount of energy was being deposited (see Figure 4.2). Later, this histogram was altered to look at only the *number* of secondary particles being

¹See Appendix B for the fluka card

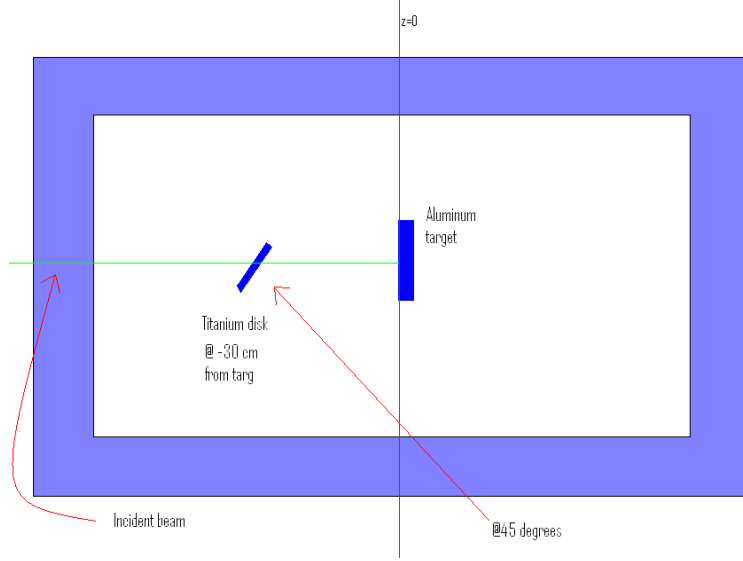


Figure 4.1: Geometry specified in fluka card.

deposited in the x-y plane (Figure 4.3) and scaled to a ratio per incident proton. Several plots were given showing the number of the 4 most important secondary particles for neutrino production: protons, neutrons, pions and kaons (Figure 4.3)². For all simulations, first generation protons and resultant photons were ignored.

Once the number of particles and the total energy profile was known, the target, approximated by an aluminum plate as specified above, was written in and more simulations were run to see what damage (if any) the stuck OTR arm would yield. Since fluka naturally gives the output in GeV/cm^3 , it was then weighted per incident proton and then converted to rads/year ³, assuming 3.3×10^{14} protons per pulse and 10^7 pulses per year. Again, incident protons and resultant photons were ignored.

While the largest amount of radiation deposited was at or around the centre, there was also a fairly large (10^2 Gy/year or greater) dosage to the target as a whole that was not seen in cases without the OTR arm. Figure 4.4 shows the difference in radiation dosage in rads/year from with the stuck OTR arm to without.

²These results were later corroborated by independent simulations done in GEANT3 at UofT.

³100 rads = 1 Gy

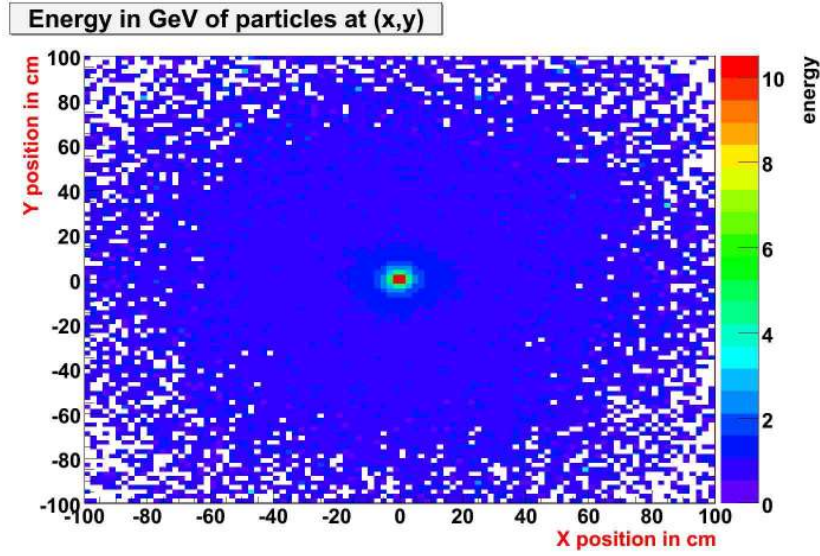


Figure 4.2: Energy profile of particles being deposited at position (x,y) 30cm from the OTR foil position.

4.2 Conclusions

The radiation exposure to the target as a result of a stuck OTR arm is considered not to be problematic. While a radiation dose of 250 Gy/year⁴ can be damaging to electronics, it was reasoned to not be of serious concern to the metal and ceramic of the target. While the damage done by a stuck OTR arm would not be enough for serious concern, a drop away feature was still included for the sake of prudence.

⁴This is the amount expected near the OTR camera.

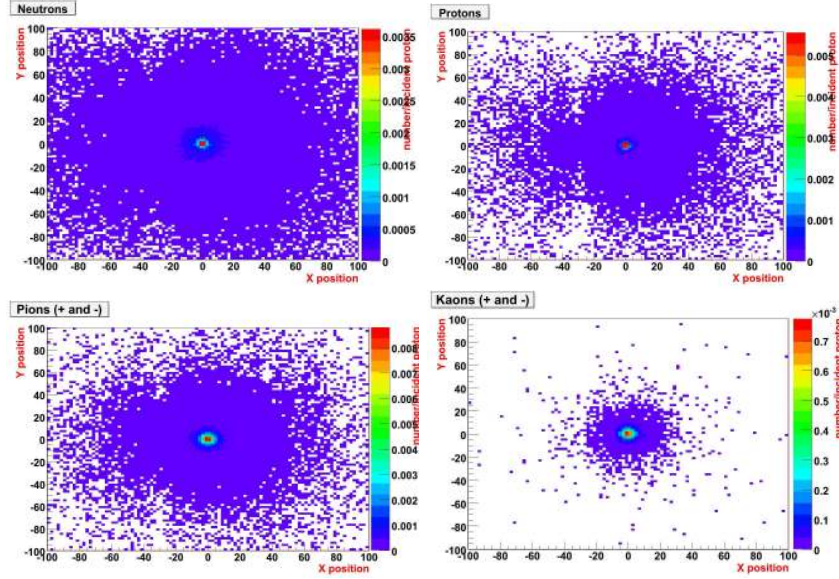


Figure 4.3: Secondary particles being deposited at position (x,y) 30cm from the OTR foil position.

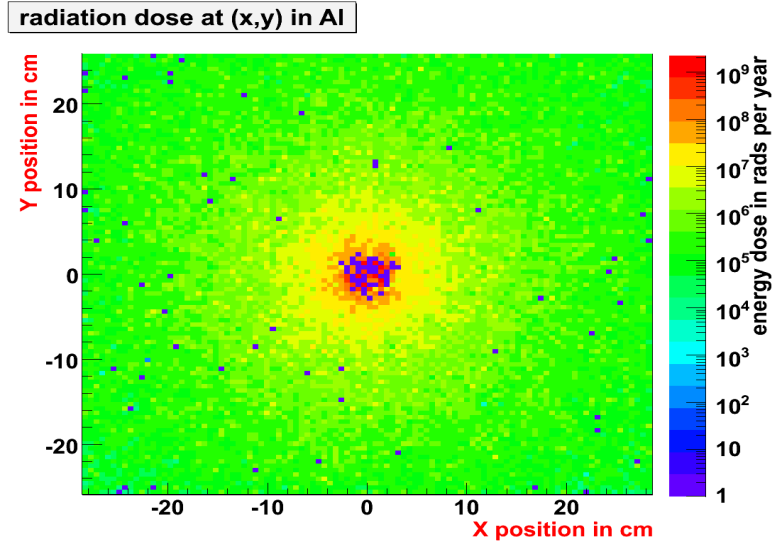


Figure 4.4: Additional radiation dosage to target in rads/year resulting from stuck OTR arm. The unobstructed beam radiation has been subtracted off.

Chapter 5

Conclusions

With the OTR system fully installed by December 2008, camera tests completed, motor controls implemented and simulations done, the OTR team is on schedule to be ready for when the beam turns on April 6, 2009 [15] [11]. While data collection can begin almost immediately thereafter, because of the difficulty in detecting neutrinos (see Section 1.2.5) coupled with the probabilities of muon neutrino disappearance (see Section 1.1), meaningful event rate (ie. number of events that can be positively identified as being electron/muon/tau neutrinos) may be low and it will still be some time before meaningful results can be produced.

It is hoped by all members of T2K, including the OTR team, that information gathered during the course of the experiment will be used in completing the Standard Model.

Appendix A

Two different GUIs were written to control the motors: the Arm Motor controller, used to rotate the disk and select the foils, and the Motor Controller, used to move the camera stage. While both use a different, but similarly styled user interface, they were largely built on the same framework. Below are portions of the header file framework with documentation added from the code itself.

Connect Class:

```
public:
Connect(void);
~Connect(void);

//public methods to be used by anyone

/*****
*gets the value of hDB and hKey (private class variables)
*returns 1 if successful, 0 otherwise - starts connection
*odbPath is a char array specifying path in odb
*****/
int makeConnection(char odbPath[50]);

/*****
*sets limit polarity of motor at index motornum
*returns a 1 if successful, 0 otherwise
*vars: motornum is index of motor (1-4)
limpol is new limit polarity (must be 1 or -1)
*****/
int setLimitPolarity(INT limpol, int motornum);

/*****
*sets velocity of motor at index motornum
*to vel
*returns a 1 if successful, 0 otherwise
*vars: motornum is index of motor (1-4)
vel is the new velocity setting
*****/
int setVelocity(float vel, int motornum);

/*****
*sets acceleration of motor at index motornum
*to acc
*returns a 1 if successful, 0 otherwise
```

```

*vars: motornum is index of motor (1-4)
acc is the new acceleartion setting
*****/
int setAcceleration(float acc, int motornum);

/*****
*returns the current position of the motor (no error handling)
*vars: motornum is index of motor desired (1-4)
*****/
float getPos(int motornum);

/*****
*returns the current 'home' limit setting of the motor
*(no error handling)
*vars: motornum is index of motor desired (1-4)
*****/
BOOL getHome(int motornum);

/*****
*rotates the motor by a given number of degrees
*vars: degree is the desired number of degrees
* motornum is the index of motor to move
*returns 1 if successful, 0 otherwise
*****/
int Rotate(float degree, int motornum);

/*****
*resets the postion of a constantly rotating motor back
*to zero
*vars: motornum is the index of the motor to reset
* this will usually always be the arm motor
*returns new postion
*****/
void resetPos(float newpos, int motornum);

/*****
*returns the degrees rotation of the current position
*from zero position
*vars: pos is position to convert to degrees
* motornum is for the motor index (most likely
* always the first one)
*returns: float of current degrees
*****/
float postoDegree(float pos, int motornum);

/*****

```



```

*checks position of motornum (typically 1)
*and sets it if motornum < - GEAR
*****/
void setPos(int motornum);

/*****
*Gets the value in Analog (under variables)
*for motor motornum: this will be the pressure
*gauge for the motor
*vars: motornum is the index of the motor
*returns the value of Analog variable (pressure
*gauge)
*-----THIS METHOD IS ONLY IMPLEMENTED FOR
*-----MOTOR ARM!!!
*****/
float GetAnalog(int motornum);

/*****
*sets the home switch to true... only available for arm motor
*-----THIS METHOD IS NOT IN THE REGULAR MOTOR
*-----CONTROLLER CODE!!!-----
*****/
void setHome();

/*****
*sets the pressure home switch to true... only available for
*arm motor
*-----THIS METHOD IS NOT IN THE REGULAR MOTOR
*-----CONTROLLER CODE!!!-----
*****/
void setPHome();

/*****
*sets the pressure threshold for the arm motor...
*to be used with PHome setting
*-----THIS METHOD IS NOT IN THE REGULAR MOTOR
*-----CONTROLLER CODE!!!-----
*****/
void setPressThresh(float thresh);

/*****
*returns the current limit polarity of motor at index
*motornum
*vars: motornum is the index of motor
*****/
INT GetLimPol(int motornum);

```

```

/*****
*returns the current velocity of motor at index
*motornum
*vars: motornum is the index of motor
*****/
float GetVelocity(int motornum);

/*****
*returns the current acceleration of motor at index
*motornum
*vars: motornum is the index of motor
*****/
float GetAcceleration(int motornum);

/*****
*returns the current pressure threshold of motor
*-----THIS METHOD IS NOT IN THE REGULAR
*-----MOTOR CONTORLLER CODE!!!!-----
*****/
float GetPressThresh();

private:
//private methods to be used by Connect class only

/*****
*Checks to see if the motor is already at new dest or not
*returns true if it isn't, false if it is (canMove? True/false)
*vars: newdest is float value of new position
* motornum is the motor number (1-4)
* -----THIS IS A PRIVATE METHOD!!-----
*****/
bool canMove(float newdest, int motornum);

/*****
*allows user to set destination
*returns 1 if successful, 0 otherwise
*vars: newdest = new destination for motor
* motornum = motor number (1-4)
*-----THIS IS A PRIVATE METHOD!-----
*****/
int setDest(float newdest, int motornum);

/*****
*moves the motor at index motornum
*returns a 1 if successful, 0 otherwise

```

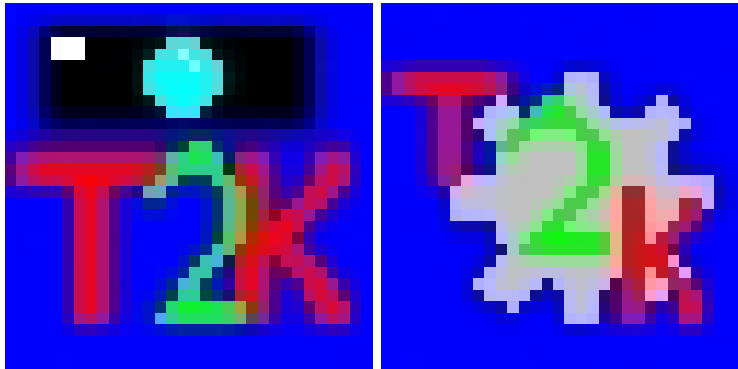


Figure 5.1: Icons for the Motor Controller and Arm Motor Controller respectively.

```
*vars: motornum is index of motor (1-4)
*-----THIS IS A PRIVATE METHOD-----
*****/
void move(int motornum);

/*****
*if tells if motor is moving
*vars: motornum is the index of the motor
*returns true or false depending on if the motor's
*still in motion or not
*-----THIS IS A PRIVATE METHOD
*****/
BOOL isMoving(int motornum);
```

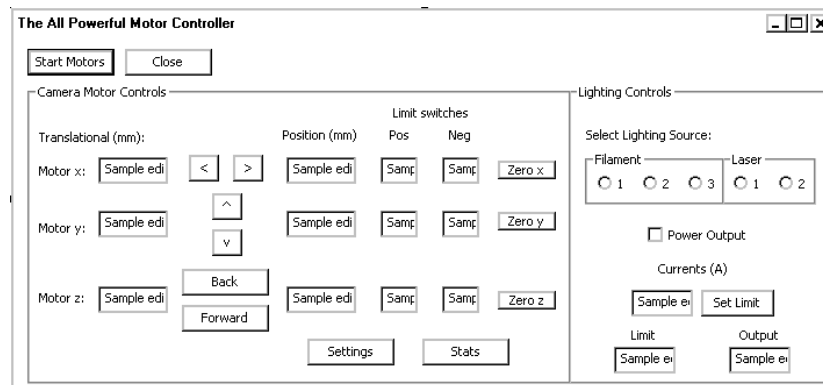


Figure 5.2: Dialog box design of Motor and Light Source Controller.

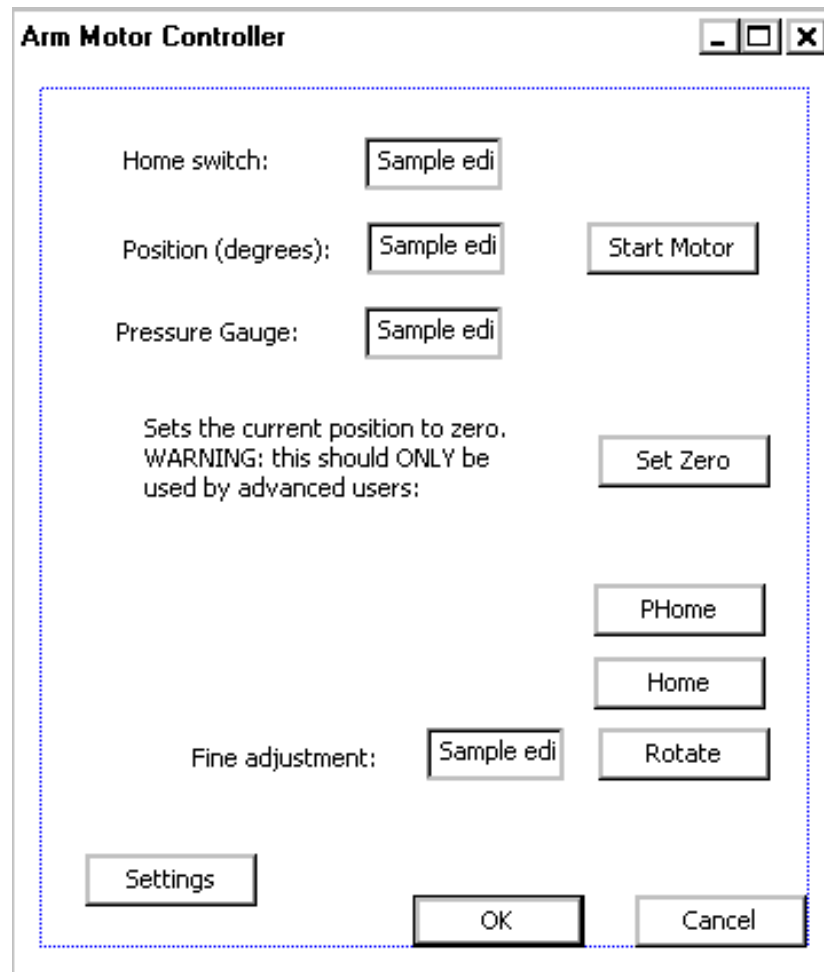


Figure 5.3: Dialog box design of Arm Motor.

Appendix B

```

*...+....1....+....2....+....3....+....4....+....5....+....6....+....7....+....8
TITLE
Particle production upon proton beam striking a titanium disk
DEFAULTS
NEW-DEFA
*...+....1....+....2....+....3....+....4....+....5....+....6....+....7....+....8
* Gaussian beam, sigma = 7.5mm
BEAM      -40.0      0.0      0.0      -1.766      -1.766      1.0 PROTON
BEAMPOS      0.0      0.0      -50.0
*...+....1....+....2....+....3....+....4....+....5....+....6....+....7....+....8
* Switch off EM showering to lower computing time
EMF
EMF-OFF
*
*...+....1....+....2....+....3....+....4....+....5....+....6....+....7....+....8
GEOBEGIN
COMBNAME
0 0
A simple Ti target inside vacuum
RPP body1 -5000000.0 +5000000.0 -5000000.0 +5000000.0 -5000000.0 +5000000.0
RPP body2 -1000000.0 +1000000.0 -1000000.0 +1000000.0 -1000.0 +1000000.0
*...+....1....+....2....+....3....+....4....+....5....+....6....+....7....+....8
*titanium disk
RCC targ      0.0      0.0      -30.0      0.0      0.59      0.59
11.25
XYP body3      0.0
*target
RPP body4      -28.5      28.5      -26.0      26.0      0.0      2.0
*minus hole in target
*RCC body5      0.0      0.0      0.0      0.0      0.0      2.0
*
0.3
*...+....1....+....2....+....3....+....4....+....5....+....6....+....7....+....8
END
* black hole
regBH1 5 +body1 -body2
* vacuum around
regVA2 5 +body2 +body3 -targ
regVA3 5 +body2 -body3 -body4
*titanium disk
regTAR 5 +targ
*aluminum target
regET 5 +body4
END
GEOEND
MATERIAL      6.0 12.0107 1.81 6.0 0.0 0.0 CARBON
*...+....1....+....2....+....3....+....4....+....5....+....6....+....7....+....8
* External Black Hole

```

```

ASSIGNMAT BLCKHOLE regBH1
* Vacuum regions
ASSIGNMAT VACUUM regVA2
ASSIGNMAT VACUUM regVA3
* titanium disk
ASSIGNMAT TITANIUM regTAR
* aluminum target
ASSIGNMAT ALUMINUM regET
*...+...1...+...2...+...3...+...4...+...5...+...6...+...7...+...8
* cartesian binning of the deposited energy inside the aluminum target
USRBIN      10.0      208.0      51.0      28.6      26.1      2.1      Edeposit
USRBIN      -28.6      -25.9      -0.1      100.0      100.0      1.0      &
* Boundary crossing current (one-way)
*
*USERDUMP      101.0      2.0      BMPI
USERDUMP      101.0      2.0      1.0      BMPI
*...+...1...+...2...+...3...+...4...+...5...+...6...+...7...+...8
RANDOMIZE      1.0
*...+...1...+...2...+...3...+...4...+...5...+...6...+...7...+...8
* Activate user dependent initialization
USRICALL
* Activate user dependent output
USROCALL
* Request a run of 100000 particles
START      25000.0
STOP

```

Bibliography

- [1] *Super-Kamiokande* Kamioka Observatory, ICRR University of Tokyo, 2007. <http://www-sk.icrr.u-tokyo.ac.jp/sk/index-e.html> Accessed: August, 2008.
- [2] Amsler, C. et al. *Particle Physics Booklet* Physics Letters B667, 1. 2008.
- [3] Backer, B. et al, *Characterization of a CID-38 Charge Injection*. SPIE Proceedings 2654, 35, 1996. <http://www.cis.rit.edu/research/CID/SJ96/paper.htm>
- [4] Berry, R., *Testing QSI's 532ws Scientific CCD Camera*. Astronomy Technology Today, Vol 2 Issue 2, February 2008. <http://www.wvi.com/~rberry/astronomy/qsitestesting/qsitestesting.htm>
- [5] Cadabeschi, M., et al. *Technical Design Report for the T2K Optical Transition Radiation Monitor* August 1, 2007.
- [6] Casper, D. *Super-Kamiokande at UC Irvine* <http://www.ps.uci.edu/~superk/>
- [7] Corlan, R., *Digital Camera Exposure Indices*. 2006. http://www.visionresearch.com/uploads/docs/Documents/WP_digexp.pdf
- [8] Coulombe, J. et al, *T2K ND280 Conceptual Design Report* T2K internal document. Version 1.0, November 6, 2005.
- [9] Eidelman, S. et al, *Neutrino mass, mixing and flavour change* Physics Letters B 592, Chapter 15 2004. Revised September 2005.
- [10] Fernow, R. *Introduction to experimental particle physics* Cambridge University Press. 1992.
- [11] Galymov, V., *Private communications* 2008.
- [12] Gitter, B. *Optical Transition Radiation* 1992 <http://pbpl.physics.ucla.edu/docserver/authors/show/3736>
- [13] Itow, Y, et al, *The JHF-Kamioka Neutrino Project* hep-ex/0106019v1, Jun 5, 2001.

- [14] Kato, I. *Status of the T2K Experiment* T2K internal document. Neutrino '08, May 27, 2008. <http://www2.phys.canterbury.ac.nz/~jaa53/>
- [15] Kato, I. *Status of T2K Experiment* The XXIII International Conference on Neutrino Physics and Astrophysics (Neutrino 2008)
- [16] Marino, A., *Update on OTR Monitor* December 2008.
- [17] Marino, A., *Private Communications* 2008.